JEM Journal of Experimental Medicine

ARTICLE

IL-17–induced HIF1α drives resistance to anti–PD-L1 via fibroblast-mediated immune exclusion

Xing Chen[1*], Junjie Zhao[1*], Tomasz Herjan[1*], Lingzi Hong[1*], Yun Liao[1], Caini Liu[1], Kommireddy Vasu[2], Han Wang[1,6,7,8], Austin Thompson[3], Paul L. Fox[2], Brian R. Gastman[1,4,5], Xiao Li[6,7,8], and Xiaoxia Li[1]

Increasing evidence suggests that intratumoral inflammation has an outsized influence on antitumor immunity. Here, we report that IL-17, a proinflammatory cytokine widely associated with poor prognosis in solid tumors, drives the therapeutic failure of anti–PD-L1. By timing the deletion of IL-17 signaling specifically in cancer-associated fibroblasts (CAFs) in late-stage tumors, we show that IL-17 signaling drives immune exclusion by activating a collagen deposition program in murine models of cutaneous squamous cell carcinoma (cSCC). Ablation of IL-17 signaling in CAFs increased the infiltration of cytotoxic T cells into the tumor mass and sensitized otherwise resistant cSCC to anti–PD-L1 treatment. Mechanistically, the collagen deposition program in CAFs was driven by IL-17–induced translation of HIF1α, which was mediated by direct binding of Act1, the adaptor protein of IL-17 receptor, to a stem-loop structure in the 3′ untranslated region (UTR) in *Hif1α* mRNA. Disruption of Act1's binding to *Hif1α* mRNA abolished IL-17–induced collagen deposition and enhanced anti–PD-L1–mediated tumor regression.

Introduction

Studies from the past decade have uncovered compelling associations between high levels of intratumoral or serum IL-17 and poor prognosis in a variety of solid tumors, especially those of mucosal origin such as cutaneous squamous cell carcinoma (cSCC) and head and neck SCC (Chen and Chen, 2014; Gopalakrishnan et al., 2018; Gu et al., 2012; He et al., 2011; Huang et al., 2014; Punt et al., 2016; Punt et al., 2015; Tosolini et al., 2011; Wu et al., 2012; Xu et al., 2014; Yan et al., 2014; Zhang et al., 2012; Zhang et al., 2013; Zhang et al., 2018). These clinical correlations have catalyzed a body of literature demonstrating a protumorigenic role for IL-17 in multiple organs in early tumorigenesis. However, the unmet medical need in cancer care primarily stems from the therapy resistance in late-stage cancer patients, whose tumor cells and tumor microenvironment (TME) are considerably different from early-stage tumors. How IL-17 affects the therapeutic response in late-stage tumors is poorly understood.

Checkpoint inhibitors are gradually becoming the first-line therapy for a variety of late cancers. By blocking the inhibitory signal (i.e., PD-1/PD-L1 axis), checkpoint inhibitors rejuvenate so called dysfunctional tumor-reactive T cells, thereby reinvigorating the antitumor immunity (Robert, 2020). However, despite its clinical success, a substantial fraction of patients do not respond to the treatment (Binnewies et al., 2018; Kim et al., 2018; Sharma et al., 2017). There is growing interest in understanding how TME influences checkpoint inhibitor–mediated antitumor immunity (Mariathasan et al., 2018; Peng et al., 2020). Most notably, the inflammatory characteristics of the TME are emerging as a critical determinant that affects the antitumor immunity induced by checkpoint inhibitors.

As an evolving concept, available evidence suggests that intratumoral inflammation can be either immunosupportive or immunosuppressive. Immunosupportive inflammation is characterized by the infiltration of CD8 T cells and dendritic cells, which are believed to be required for checkpoint inhibitor–mediated tumor regression. Immunosuppressive inflammation, often associated with prolonged wound healing responses in chronically inflamed tissues, features the presence of regulatory immune cells and desmoplastic reaction that can blunt antitumor immunity. While we have previously shown that IL-17 plays a critical role in the wound healing process in the skin (Chen et al., 2019), a number of studies have linked elevated IL-17 levels

[1]Department of Inflammation and Immunity, Lerner Research Institute, Cleveland Clinic, Cleveland, OH; [2]Department of Cardiovascular and Metabolic Sciences, Lerner Research Institute, Cleveland Clinic, Cleveland, OH; [3]School of Medicine, Case Western Reserve University, Cleveland, OH; [4]Department of Dermatology, Cleveland Clinic, Cleveland, OH; [5]Department of Plastic Surgery, Cleveland Clinic, Cleveland, OH; [6]Department of Biochemistry, School of Medicine, Case Western Reserve University, Cleveland, OH; [7]Center for RNA Science and Therapeutics, School of Medicine, Case Western Reserve University, Cleveland, OH; [8]Department of Computer and Data Sciences, School of Engineering, Case Western Reserve University, Cleveland, OH.

*X. Chen, J. Zhao, T. Herjan, and L. Hong contributed equally to this paper. Correspondence to Xiao Li: xiao.li9@case.edu; Xiaoxia Li: lix@ccf.org.

with immunosuppressive TME (Han et al., 2014; Zhang et al., 2020). In support of this, data from correlative analyses of clinical specimens have implicated IL-17 in therapeutic resistance against checkpoint inhibitors in lung, colorectal, melanoma, and breast cancer patients (Chen and Chen, 2014; Gopalakrishnan et al., 2018; Gu et al., 2012; He et al., 2011; Huang et al., 2014; Punt et al., 2016; Punt et al., 2015; Tosolini et al., 2011; Wu et al., 2012; Xu et al., 2014; Yan et al., 2014; Zhang et al., 2012; Zhang et al., 2013; Zhang et al., 2018). Nevertheless, the mechanism underlying the immunosuppressive function of IL-17 remains unclear.

Here, we describe a previously underappreciated mechanism by which IL-17 drives the therapeutic failure of anti–PD-L1. We found that IL-17 signaling in cancer-associated fibroblasts (CAFs) activated a collagen deposition program in murine models of cSCC. IL-17–activated CAFs formed thick layers of tumor stroma that effectively trapped cytotoxic T cells, insulating the tumor cells from antitumor immune response. Ablation of IL-17 signaling in CAFs increased the infiltration of cytotoxic T cells into the tumor mass and sensitized otherwise resistant cSCC to anti–PD-L1 treatment. Mechanistically, we found that the collagen deposition program in CAFs was driven by IL-17–induced translation of HIF1α, which was mediated by direct binding of Act1, the adaptor protein of IL-17 receptor, to a stem-loop structure in the 3′ UTR in the *Hif1α* mRNA. Lastly, we showed that specific disruption of Act1's binding to *Hif1α* mRNA abolished IL-17–induced collagen deposition and enhanced anti–PD-L1–mediated tumor regression.

Results

Fibroblast-specific deletion of IL-17RC enables anti–PD-L1–mediated tumor regression

At late stage of the 7,12-dimethylbenz[a]anthracene (DMBA)/12-*O*-tetradecanoylphorbol-13-acetate (TPA) model in established skin tumors, tumor cells were encapsulated as islets by thick layers of stroma comprised of fibronectin-positive CAFs (Fig. 1 Aa). Intriguingly, IL-17–producing cells were predominantly found in the tumor stroma of the DMBA/TPA model (Fig. 1 Aa). IL-17–producing cells were readily detectable in the tumors treated with immune checkpoint inhibitors (e.g., anti–PD-L1; Fig. 1 Ab). This observation prompted us to assess the role of CAF-intrinsic IL-17 signaling in the DMBA/TPA model in the context of immune therapy with checkpoint inhibitors.

To this end, we generated tamoxifen (TAM)-inducible fibroblast-specific IL-17RC–deficient mice (IL-17RC$^{f/f}$ Col1a2^{CreERT2}) and control mice (IL-17RC$^{f/+}$Col1a2^{CreERT2}). To achieve IL-17RC deletion in CAFs, the experimental mice were subjected to DMBA/TPA treatment for 18 wk followed by TAM exposure (Fig. 1 B), which led to an ablation of IL-17 signaling in CAFs derived from the DMBA/TPA-induced tumors (Fig. 1 C). Consistent with a profibrotic role for IL-17, deletion of IL-17RC from the CAFs reduced collagen deposition in the tumor (Fig. 1 D). The reduced collagen deposition did not halt or hinder tumor growth (Fig. 1 E). However, ablation of IL-17 signaling in CAFs sensitized DMBA/TPA-induced tumors to anti–PD-L1–mediated tumor regression (Fig. 1 E), which were otherwise resistant to the checkpoint inhibitor treatment (Fig. 1 E).

To further validate this finding, we implanted PDVC57 cells, a murine SCC cell line (Buchmann et al., 1991; Quintanilla et al., 1991), into the flanks of IL-17RC$^{f/f}$Col1a2^{CreERT2} and control mice to establish syngeneic tumors (Fig. 1 F). In this model, anti–PD-L1 treatment upregulated the expression of IL-17A (Fig. 1 I) in the tumor and induced a dense layer of collagen-laden CAFs (Fig. 1 G), which slightly retarded tumor growth (Fig. 1 H). To abrogate IL-17 signaling in CAFs, we administered three doses of TAM to each tumor-bearing mouse over the duration of anti–PD-L1 treatment (Fig. 1 F). Deletion of IL-17RC in CAFs did not alter the growth kinetics of the implanted tumors (Fig. 1 H), but it allowed anti–PD-L1 treatment to substantially subdue tumor growth and reduce tumor volume (Fig. 1 H). Of interest, IL-17RC is used by both IL-17A and IL-17F. To define the specific contribution of IL-17A, we tested the impact of IL-17A neutralization on anti–PD-L1–induced tumor regression in the PDVC57 model (Fig. S1). Consistent with prior reports, combined therapy of IL-17A neutralization and anti–PD-L1 was able to contain the growth of PDVC57 tumor, resulting in slight regression of the tumor size, whereas tumors treated with anti–PD-L1 monotherapy continued to grow (Fig. S1 A). Importantly, IL-17A neutralization was sufficient to suppress the expression of HIF1α as well as collagen deposition and improved the infiltration of CD8 T cells in the tumor (Fig. S1, B–D). Taken together, the data indicated that ablation of IL-17A–induced signaling in CAFs sensitized cutaneous SCCs to anti–PD-L1–mediated tumor regression.

IL-17 signaling in CAFs establishes an immune exclusion zone that insulates tumor cells

Intriguingly, despite the lack of response in the control mice IL-17RC$^{f/+}$Col1a2^{CreERT2} in the DMBA/TPA model, anti–PD-L1 treatment did increase the number of granzyme-producing CD8 T cells in stroma of tumors (Fig. 2 A). However, the infiltrating CD8 T cells appeared to be trapped in the tumor stroma, as very few CD8 T cells could be found inside the tumor mass (Fig. 2, A and B). CAF-specific deletion of IL-17 signaling led to a pronounced increase in the number of infiltrations of CD8 T cells in the tumor mass in response to anti–PD-L1 in both the DMBA/TPA model and PDVC57 tumors (Fig. 2, A–D), which was accompanied by reduced collagen deposition (Figs. 1 D and 2 E). Furthermore, flow cytometry analysis of dissociated whole tumor also showed an increase in the total number of granzyme B$^+$ CD8 T cells in anti–PD-L1–treated tumors from IL-17RC$^{f/f}$Col1a2^{CreERT2} compared with control (Fig. 2 F). The frequency of Ki67$^+$ CD8 T cells was slightly increased upon IL-17RC deletion, and was further elevated by anti–PD-L1 treatment (Fig. S1 F). Imaging analysis revealed that tumor-infiltrating CD8 T cells in anti–PD-L1–treated IL-17RC$^{f/f}$Col1a2^{CreERT2} mice were redistributed to the tumor islets and exhibited a higher frequency of Ki67 expression compared with those from the control mice (Fig. 2 G). Of note, Gr1$^+$ myeloid cells in the tumor tissue were comparable in anti–PD-L1–treated IL-17RC$^{f/f}$ Col1a2^{CreERT2} and control mice (Fig. 2 H).

To test whether the increased infiltration of CD8 T cells contributed to the improved therapeutic response, we depleted CD8 T cells in IL-17RC$^{f/f}$Col1a2^{CreERT2} mice before and during

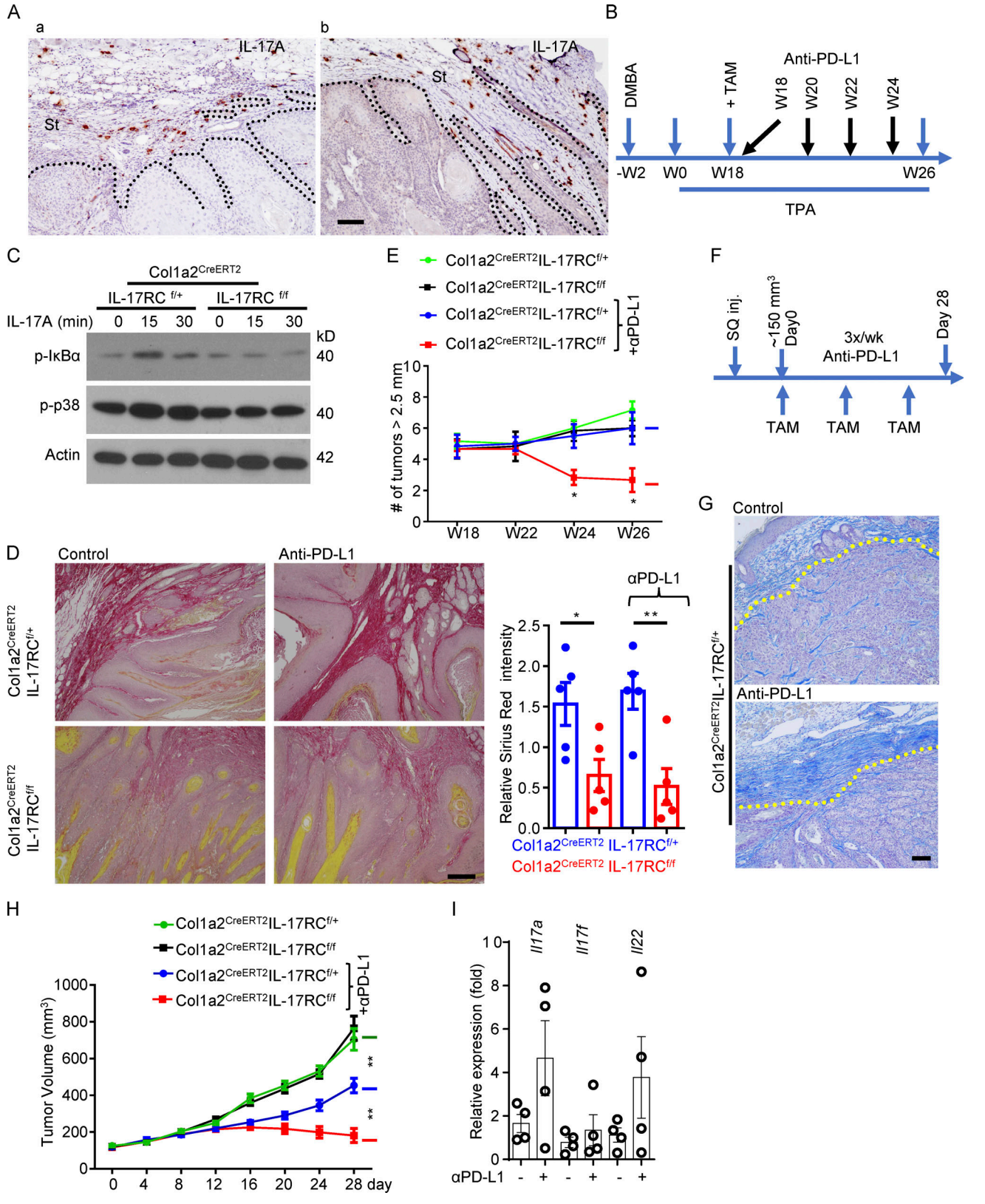

Figure 1. **Ablation of IL-17 signaling in fibroblasts sensitizes cutaneous SCC to anti–PD-L1–mediated regression. (A)** Representative images of IL-17A expression (immunohistochemical staining) in established tumors induced by DMBA/TPA alone (a) or tumors induced by DMBA/TPA combined with anti–PD-L1 treatment (b). St, stroma area. **(B)** Treatment schedule of DMBA/TPA model for experiments in C–E. **(C)** CAFs of DMBA/TPA-induced tumors from IL-17RC$^{f/+}$Col1a2^{CreERT2} and IL-17RC$^{f/f}$Col1a2^{CreERT2} mice (harvested and expanded at the endpoint of this model) were treated with IL-17A followed by Western analysis of IL-17 response. **(D)** Representative images of Sirius Red staining to show the collagen deposition of the DMBA/TPA-induced tumors from indicated mice. Bar graph shows relative intensity of Sirius Red–stained collagen from random area of five independent tumors. Error bars represent ± SEM. *, P < 0.05;

, P < 0.01 by *t* test. **(E) Total number of tumors (≥2.5 mm in diameter) per mouse from DMBA/TPA model over the time course of DMBA/TPA model described in B. Mice with similar tumor burden (six mice in each group) were selected and randomly grouped at week 18 for TAM induction and further anti–PD-L1 treatment. *, P < 0.05 by *t* test at indicated time points. Error bars represent ± SEM. Data are representative of two independent experiments. **(F)** Treatment schedule for PDVC57 tumor model–based experiments in G–I. SQ inj., subcutaneously injected. **(G)** Control and anti–PD-L1 treated PDVC57 tumors from endpoint of IL-17RC$^{f/+}$Col1a2^{CreERT2} mice of F were characterized for extensive stroma using aniline blue staining. **(H)** Graph shows the tumor volumes of PDVC57 model described in F. Mice with similar tumor size (~150 mm^3, five mice in each group) were selected for TAM induction and further anti–PD-L1 treatment. **, P < 0.01 by *t* test for the indicated groups at the endpoint. Error bars represent ± SEM. Data are representative of two independent experiments. **(I)** Relative mRNA levels of indicated genes in PDVC57 tumors treated with or without anti–PD-L1 from IL-17RC$^{f/+}$Col1a2^{CreERT2} mice. *n* = 4 biological samples each group. Error bars represent ± SEM. Scale bars for A and G = 100 µm; D = 200 µm. α is used for "anti-" in bar graphs throughout. Dotted lines in A and G are used to show the main boundary of tumor islets and stroma areas.

anti–PD-L1 treatment. The efficiency of CD8 T cell depletion was >90%, as shown by the frequency of splenic CD8 T cells (Fig. 3 A). CD8 T cell depletion abrogated the sensitivity to anti–PD-L1 in IL-17RC$^{f/f}$Col1a2^{CreERT2} mice (Fig. 3, B–D). Interestingly, we found that infiltrating CD8 T cells were also trapped in tumor stroma in human SCC, and the entrapment of CD8 T cells correlated with intratumoral IL-17 levels (Fig. 3, E and F). Taken together, our data show that IL-17 signaling in CAFs promotes resistance to checkpoint inhibitors by hindering cytotoxic T cell infiltration into tumor mass.

IL-17 induces a collagen deposition program in CAFs by promoting the expression of HIF1α

Next, we sought to determine the mechanism by which IL-17 signaling in CAFs promotes the exclusion of CD8 T cells. While IL-17 is well known for its ability to induce the expression of chemokines and cytokines, we noticed that ablation of IL-17 signaling in CAFs led to a reduction in CAF proliferation and collagen production (Figs. 1 D, 2 E, and S2 A). Intriguingly, while IL-17 signaling has been shown to activate fibroblasts in secondary lymphoid tissues and drive their proliferation through metabolic reprogramming (Majumder et al., 2019), the nexus between IL-17 activity and collagen deposition is poorly understood. The deposition of collagen requires not only the synthesis of procollagen peptides but also also a series of posttranslational modifications required for proper collagen deposition. Before secretion into the extracellular space, procollagen-proline dioxygenase (P4Hs, including P4HA1-3 and P4HB) catalyzes the hydroxylation of proline to facilitate the folding and assembly of procollagen; secreted procollagen is then crosslinked by lysyl oxidases (LOXs), giving rise to collagen fibers (Malhotra and Erlmann, 2015; Myllyharju, 2003; Rossow et al., 2018; Vallet and Ricard-Blum, 2019). Importantly, both the P4Hs and LOX are transcriptional targets of HIF1α (Bentovim et al., 2012; Myllyharju, 2008).

We found that fibroblast-specific deletion of IL-17RC markedly reduced the expression of HIF1α, P4Hs, and LOX in the tumors (Fig. 4 A). Consequently, there was a substantial reduction in hydroxylated collagen, and the activity of LOX was also diminished in the IL-17RC$^{f/f}$ Col1a2^{CreERT2} mice compared with control (Fig. 4, B and C). Because both the P4Hs and LOX are transcriptional targets of HIF1α (Bentovim et al., 2012; Myllyharju, 2008), we hypothesized that IL-17 signaling in CAFs drives the collagen deposition program by inducing the expression of HIF1α. In support of our hypothesis, knockdown of *Hif1α* in human CAFs isolated from primary SCC suppressed the expression of P4H enzyme genes as well as LOX (Fig. 4 D). To further test the hypothesis, we genetically ablated HIF1α expression by transducing Cre recombinase or GFP (control) into primary dermal fibroblasts from HIF1α$^{f/f}$ mice. Ablation of HIF1α from skin fibroblasts abrogated IL-17–induced expression of P4H enzymes and LOX (Fig. 4 E) and abolished IL-17–induced production of hydroxylated collagen as well as LOX activity (Fig. 4 F).

Importantly, treatment with IL-17A, and to a lesser extent, IL-17F, induced the expression of HIF1α and P4Hs (Fig. S1 E). IL-17A treatment increased the level of hydroxylated collagen and LOX activity in three independent lines of primary CAFs from human SCC (Fig. S3, A and B). Furthermore, HIF1α knockdown blocked the induction of P4Hs and LOX in human primary CAFs in response to IL-17 stimulation (Fig. 4 D). Additionally, immunofluorescence staining of human SCC showed a positive correlation between the presence of IL-17A$^+$ cells and HIF1α nuclear localization in tumor stromal cells (Fig. S3 C), indicating that production of IL-17 was associated with increased HIF1α activation in human SCC. Taken together, the data indicate that IL-17 induces a collagen deposition program in CAFs by promoting the expression of HIF1α in mouse and human SCC.

Notably, DMBA/TPA-induced tumors harvested 20 wk after the initiation of TPA treatment had noticeably higher levels of hydroxyl collagen and LOX activity than those collected 16 wk after treatment (Fig. S4 A), indicating that collagen continued to accumulate in the TME over the course of tumor development. Ablation of IL-17RC expression from fibroblasts diminished the accrual of hydroxylated collagen and decreased the activity of LOX compared with the 16-wk baseline (Fig. S4 A). Collectively, the data suggest that the IL-17–HIF1α axis in CAFs is required for the continued accumulation of collagen and maintenance of LOX activity in fibrotic tumor.

The adaptor protein of IL-17 signaling Act1 binds to 3′ UTR in *Hif1α* mRNA to promote its translation in response to IL-17 stimulation

Interestingly, while IL-17 stimulation upregulated the expression of HIF1α protein in primary CAFs (Fig. 5 A), the induction at protein level was not associated with a commensurate fold increase in *Hif1a* transcripts (Fig. 5 A). Notably, blockade of protein synthesis using cycloheximide not only prevented IL-17–induced HIF1α expression, but also led to a reduction of HIF1α protein, indicating that IL-17 treatment did not inhibit HIF1α degradation (Fig. 5 B). IL-17A failed to induce HIF1α expression in Act1-deficient cells restored with an Act1 RNA binding mutant,

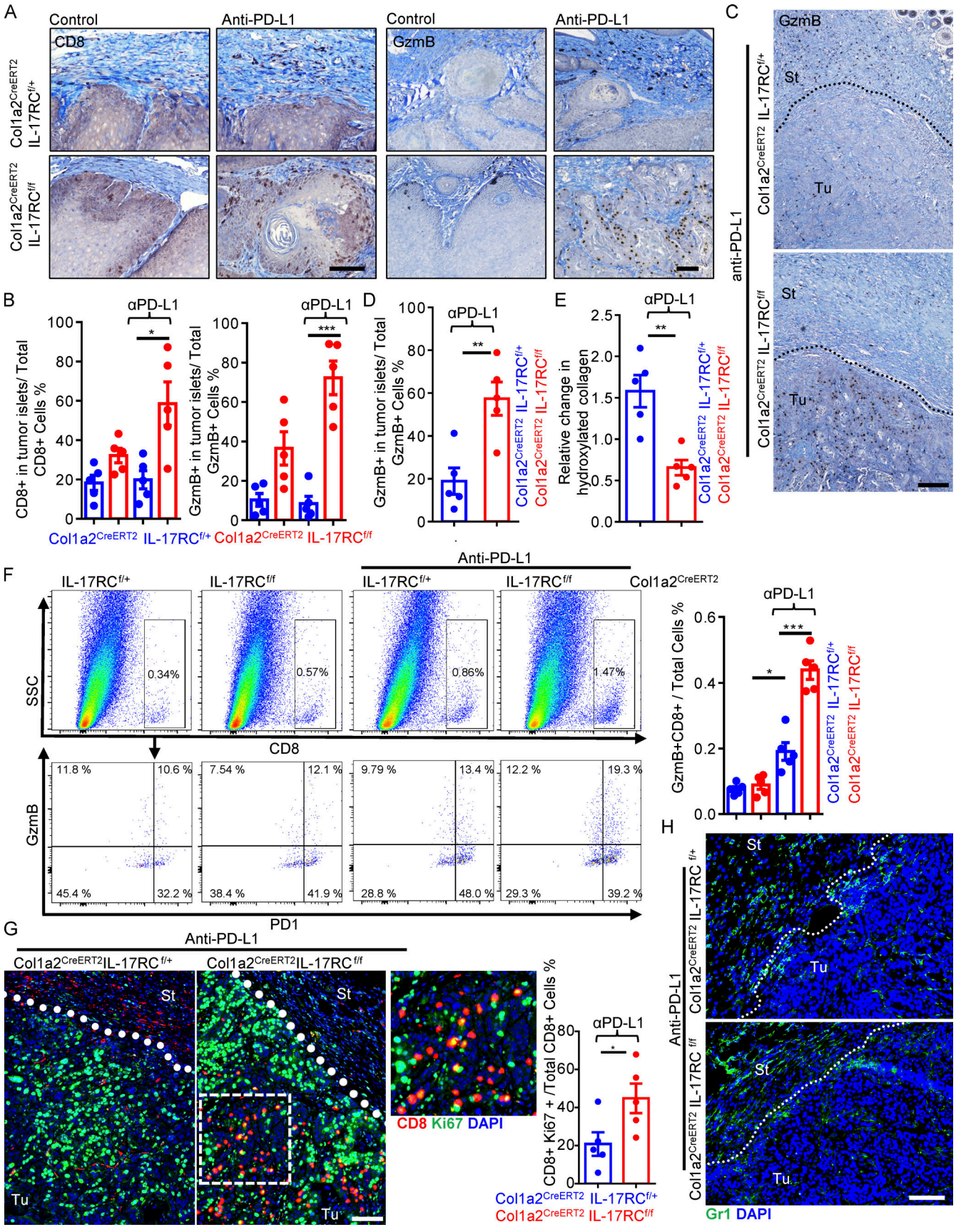

Figure 2. **Ablation of IL-17 signaling in fibroblast increases cytotoxic T cell activity in tumor islets. (A and B)** Immune staining (A) and quantification (B) of tumors for CD8 and granzyme B from indicated mice of DMBA/TPA model at week 26 (Fig. 1 E). Bar graph (B) represents CD8⁺ cell or GzmB⁺ cell ratio in the

tumor islets over total CD8⁺ or GzmB⁺ cells (in stroma and in tumor islets). Five specimens were used. Error bars represent ± SEM. *, P < 0.05; ***, P < 0.001 by *t* test. **(C and D)** Immune staining (C) and quantification (D) for granzyme B from endpoint PDVC57 tumors of Fig. 1 H. Bar graph indicates GzmB⁺ cell ratio in the tumor islets over total GzmB⁺ cells (in the stroma and in tumor islets). *n* = 5. Error bars represent ± SEM. **, P < 0.01 by *t* test. St, stroma; Tu, tumor islets. **(E)** Tumor tissue from endpoint PDVC57 tumors of Fig. 1 H were subjected to hydroxyproline assay for relative hydroxylated collagen levels. *n* = 5. Error bars represent ± SEM. **, P < 0.01 by *t* test. **(F)** Tumor tissues from endpoint of PDVC57 model as described in Fig. 1 F were harvested, dissociated, and examined by flow cytometry analysis for indicated markers. Bar graph indicates GzmB⁺CD8⁺ T cells/total cells ratio in the tumor from five independent specimens. Error bars represent ± SEM. *, P < 0.05; ***, P < 0.001 by *t* test. SSC, side scatter. **(G and H)** Immunofluorescence staining for CD8/Ki67 (G) and Gr1 (H; frozen sections) from endpoint of indicated tumors in Fig. 1 H. Bar graph indicates CD8⁺Ki67⁺/Total CD8 T cell ratio in the tumor. *n* = 5. Error bars represent ± SEM. *, P < 0.05 by *t* test. Scale bars for A, C, G, and H = 100 µm. St, stroma; Tu, tumor islets. Dotted lines are used to show the main boundary of tumor islets and stroma areas. All data in Fig. 2 are representative of two independent experiments.

SEFIR1+5mt (Fig. 5 B; Herjan et al., 2018). These data pointed to an IL-17–mediated enhanced translation of HIF1α. Indeed, ribosome fractionation revealed that *Hif1a* mRNA shifted from a translationally inactive fraction into a translationally active polyribosome fraction in response to IL-17 treatment (Fig. 5 C). A hallmark outcome of IL-17 signaling, as shown by us and others, is the activation of posttranscriptional regulation for a subset of target genes (Amatya et al., 2018; Herjan et al., 2018). We have recently reported that the SEFIR domain in Act1, the adaptor molecule for the IL-17 receptor, can directly recognize and bind to a unique stem-loop structure (termed SEFIR binding element [SBE]) in select transcripts to promote their expression (Herjan et al., 2018). By motif comparison and in vitro screening (data not shown), we identified an SBE (Fig. 5 D) in the 3′ UTR of mouse *Hif1α* mRNA. RNA electrophoretic mobility shift assays (REMSAs) confirmed that recombinant Act1 SEFIR directly bound to the HIF1α 3′ UTR SBE-containing region, whereas Act1 RNA binding mutant SEFIR1+5mt failed to bind (Fig. 5 E). In addition, RNA immunoprecipitation (RIP) showed that Act1 binds to *Hif1α* transcript upon IL-17 stimulation (Fig. 5 F). To further test the role of Act1 RNA binding in IL-17–mediated HIF1α translation, we retrovirally restored Act1-deficient primary skin fibroblasts with either a Flag-tagged wild-type Act1 or mutant Act1 that is defective in the ability to bind to mRNA (referred to as 1+5mt; Herjan et al., 2018; Fig. 5 G). Consistent with our hypothesis, IL-17–induced HIF1α protein expression as well as the expression of P4H enzymes and LOX was abolished in dermal fibroblasts expressing Act1 SEFIR1+5mt (Fig. 5 H). This was accompanied by a substantial reduction in the production of hydroxylated collagens and LOX activity (Fig. 5 I). Taken together, the data showed that IL-17 promotes the translation of HIF1α via the direct binding of Act1 to *Hif1α* mRNA.

Disruption of Act1 binding to *Hif1α* transcript sensitizes tumor to anti–PD-L1 treatment

We previously demonstrated that the interaction between Act1 and its target transcripts can be disrupted by chemically modified RNA oligos (aptamers) that share the same sequence with the SBEs in target transcripts (Herjan et al., 2018). SBE aptamers can inhibit IL-17–mediated posttranscriptional regulation both in vitro and in vivo. We generated a novel RNA aptamer (see Materials and methods) with the same sequence as that of the SBE in the 3′ UTR of *Hif1α*. This *Hif1α*-targeting aptamer displayed potent inhibitory activity against Act1 SEFIR in the REMSA assay against its binding to *Hif1α* transcript (Fig. 6 A). Transfection of *Hif1α* aptamer dramatically inhibited IL-17–induced Act1 binding to *Hif1α* mRNA (Fig. 6 B); abrogated IL-17–induced expression of HIF1α, P4H enzymes, and LOX in dermal fibroblasts (Fig. 6 C); and reduced the IL-17–induced increase in production of hydroxylated collagen and LOX activity (Fig. 6 D).

This inhibitory activity of *Hif1α* aptamer provided us with a unique tool to assess the role of the IL-17–induced collagen deposition program in immune exclusion and resistance to anti–PD-L1. Although the growth of tumors was only slightly retarded compared with those that received control aptamer without anti–PD-L1 (Fig. 6 E), combined treatment with *Hif1α* aptamer and anti–PD-L1 completely halted tumor growth and shrank the average tumor volume (Fig. 6 E). This was associated with increased infiltration of granzyme B–producing T cells in the tumor mass and reduced trapping of cytotoxic T cells in the tumor stroma (Fig. 6 F). Injection of the *Hif1α* aptamer into anti–PD-L1–treated PDVC57 tumors reduced intratumoral expression of HIF1α, P4H enzymes, and LOX (Fig. 6 G), which were accompanied by reduced overall collagen deposition, as indicated by hydroxylated collagen and LOX activity (Fig. 6 H). Interestingly, abrogation of HIF1α expression did not affect CAF proliferation (Fig. S2 B), as that found in the fibroblast-specific IL-17RC knockout mice (Fig. S2 A). In fact, HIF1α appeared to be dispensable for IL-17–induced expression of CPT1a and HK2 in skin fibroblasts (Fig. S4 B), a process previously shown to underpin the proliferative effect of IL-17 in fibroblasts in secondary lymphoid tissues (Majumder et al., 2019). In addition, the *Hif1α* aptamer did not impact the expression of signature chemokines and cytokines, such as *Tnfa*, *Il6*, *Cxcl1*, and *Ccl2* (Fig. 6 I), indicating the specific inhibitory activity of *Hif1α* aptamer against the collagen deposition program. Taken together, the data suggested that disruption of the IL-17–induced *Hif1a*-mediated collagen deposition program sensitizes otherwise resistant tumors.

Discussion

A pathogenic role of IL-17 in mediating therapeutic resistance to checkpoint inhibitors has been widely speculated and implicated in the literature (Akbay et al., 2017; Gopalakrishnan et al., 2018; Liu et al., 2021; Llosa et al., 2019; Zhang et al., 2020). However, the majority of past studies, including our own, relied on neutralizing antibody or global IL-17/IL-17 receptor–deficient mice to ablate IL-17 activity. While those studies provided a highly concrete scientific premise, due to the broad tissue spectrum of IL-17 receptor expression, the precise impact of IL-17 on tumor immunity had been elusive. Here, by timing the deletion of IL-17 receptor specifically in fibroblasts after tumor formation, we

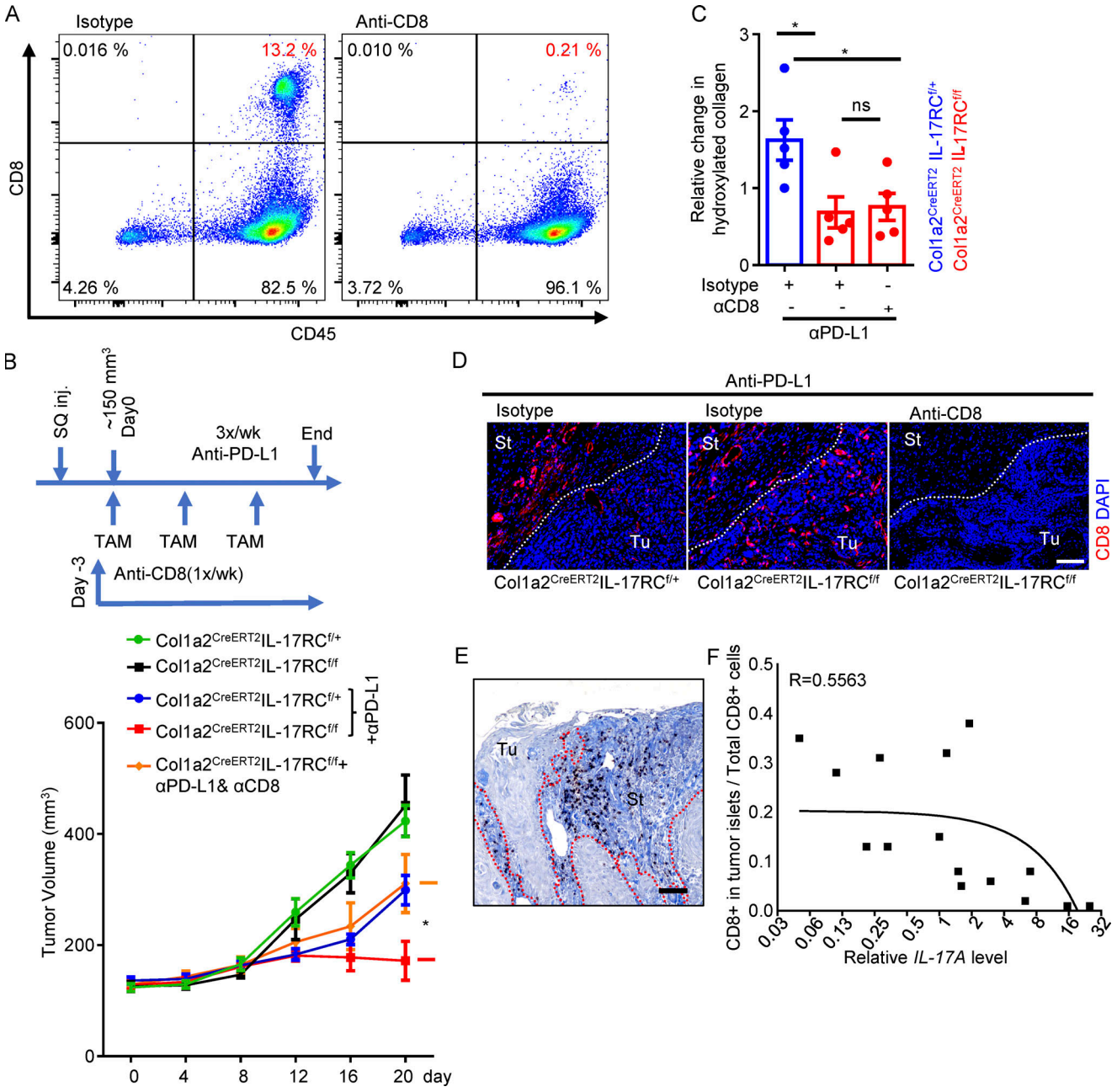

Figure 3. **CD8 depletion abrogated the sensitivity to anti–PD-L1 in IL-17RC$^{f/f}$Col1a2^{CreERT2} mice. (A)** Flow cytometry analysis of splenic CD8 cells after anti-CD8 depletion. **(B)** CD8 T cell depletion abrogated the sensitivity to anti–PD-L1 in IL-17RC$^{f/f}$ Col1a2^{CreERT2} mice. Graph presents tumor volumes from PDVC57 model over the time course. Mice with similar tumor size (~150 mm^3, five mice in each group) were selected for TAM induction and treatments of anti-CD8 and anti–PD-L1. Error bars represent ± SEM. *, P < 0.05 by *t* test for the indicated groups at the endpoint. SQ inj., subcutaneously injected. **(C)** Tumor tissue from indicated groups from B were subjected to hydroxyproline assay for relative hydroxylated collagen levels. *n* = 5 independent specimens. Error bars represent ± SEM. *, P < 0.01 by *t* test. **(D)** Representative images of CD8 staining from in indicated groups of B. Scale bar = 100 µm. Data for A–D are representative of two independent experiments. **(E)** Human cutaneous SCC sections were stained for CD8 and counterstained with aniline blue. Scale bar, 100 µm. St, stroma; Tu, tumor islets. Dotted lines in D and E are used to show the main boundary of tumor islets and stroma areas. **(F)** Graph shows correlation of immune exclusion (measured by ratio values of CD8 T cells in tumor compartments) and levels of *IL-17A* (determined by RT-PCR) in 15 randomly selected human cutaneous SCCs.

describe a previously unknown CAF-intrinsic activity of IL-17 in remodeling the tumor stroma, which directly contributes to the formation of a physical barrier that protected the tumor cells from the attack of anti–PD-L1–induced cytotoxic T cells. These findings highlight an underappreciated mechanism by which IL-17–mediated chronic and immunosuppressive inflammation interferes with therapeutic response to cancer immunotherapeutics (Fig. 7).

Chronic IL-17 activity has long been shown to promote pathological fibrosis in the intestine (Honzawa et al., 2014; Park

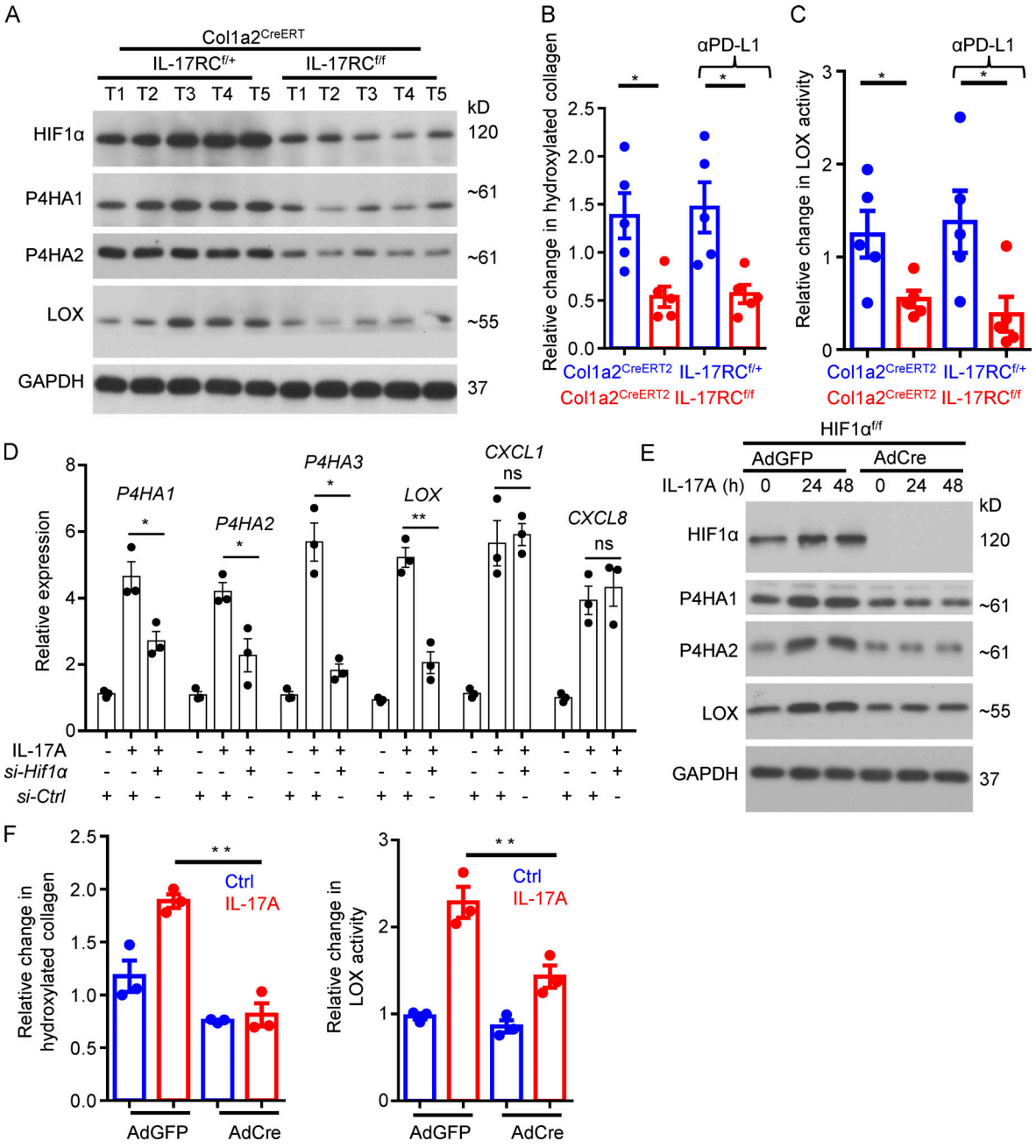

Figure 4. **IL-17–induced collagen deposition in fibroblasts through HIF1α cascade. (A)** Western analysis of indicated proteins in tumor lysates from indicated mice on DMBA/TPA model treated with anti–PD-L1 at week 26 as described in Fig. 1 B. Each lane indicates an individual sample. **(B and C)** Tumor tissues from same experiment of A were subjected to hydroxyproline assay (B) and LOX assay (C). *n* = 5 tumors. Error bars represent ± SEM. *, P < 0.05 by *t* test. Data are representative of two independent experiments for A–C. **(D)** Human SCC CAFs were subjected to *Hif1α* knockdown by transfection with *si-Ctrl* or *si-Hif1α*. Cells were then treated with IL-17A for 24 h, followed by RT-PCR analysis. Bar graph represents related gene expression level of indicated genes. *n* = 3 technical repeats. Error bars represent ± SEM. *, P < 0.05; **, P < 0.01 by *t* test. **(E and F)** Dermal fibroblasts were isolated from HIF1α$^{f/f}$ mice, followed by infection with adenovirus encoding GFP or Cre. Cells were then untreated or treated with IL-17A for indicated times, followed by Western analysis (E) or hydroxyproline assay and LOX assay (F). *n* = 3 technical repeats. Error bars represent ± SEM. **, P < 0.01 by *t* test. Data are representative of three independent experiments for D–F.

et al., 2018) and liver (Meng et al., 2012; Tan et al., 2013) in response to chronic tissue damage. Similar to our findings, IL-17 was shown to alter the cytokines released by tumor fibroblasts (Mucciolo et al., 2021; Zhang et al., 2020), mediating resistance to checkpoint blockade in pancreatic cancer (Zhang et al., 2020). By delineating the IL-17–HIF1α axis in CAFs, our findings extend these prior reports and provide a mechanistic link between IL-17 activity and pathological fibrosis. Of note, IL-17 enhances the translation of *Hif1α* mRNA by directing Act1, the adaptor protein of the IL-17 receptor, to bind to *Hif1α* transcript, which further guides *Hif1α* mRNA to polyribosomes for its translation. This mode of action potentially represents an intriguing paradigm by

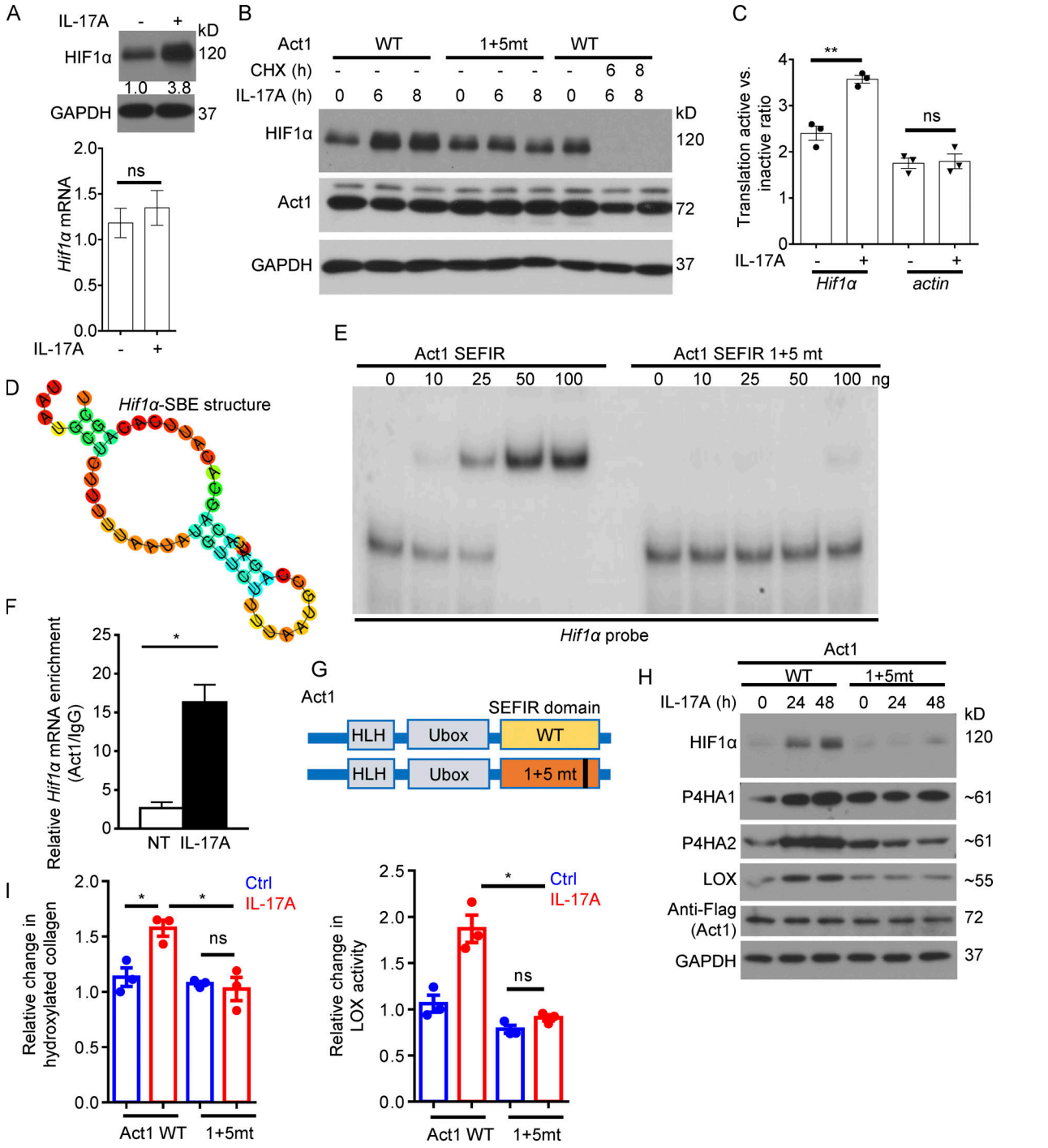

Figure 5. **IL-17 induced collagen deposition via Act1-mediated translational control of HIF1α in fibroblasts. (A)** CAFs of DMBA/TPA-induced tumors were treated with IL-17A for 8 h followed by RT-PCR and Western analysis of HIF1α expression. Numbers indicate fold-change of HIF1α protein. Bar graph shows relative *Hif1α* mRNA level. $n = 3$. Error bars represent ± SEM. *t* test. **(B)** Dermal fibroblasts from Act1-deficient mice restored with Act1 WT and Act1 RNA binding mutant (SEFIR1 + 5 mt, referred as 1+5mt) were then untreated or treated with IL-17A (with or without treatment with cycloheximide [CHX], 100 µg/ml) for 6 and 8 h, followed by Western analysis. Data are representative of at least three independent experiments for A and B. **(C)** CAFs of DMBA/TPA-induced tumors were treated with IL-17A for 8 h followed by polysome fractionation and RT-PCR. Error bars represent ± SEM. **, $P < 0.01$ by *t* test. Data are representative of two independent experiments. **(D)** Secondary-structure prediction of *Hif1α*-SEB from mouse *Hif1α* mRNA 3′ UTR (RNAfold web server, http://rna.tbi.univie.ac.at/cgi-bin/RNAWebSuite/RNAfold.cgi). **(E)** REMSA of purified recombinant Act1 SEFIR and SEFIR RNA binding mutant (1+5mt) to the mouse *Hif1α* 3′ UTR SBE-containing region (transcript position: 3,113–3,200). **(F)** Dermal fibroblasts were treated with IL-17A for 8 h followed by anti-Act1 RIP and RT-PCR for *Hif1α* mRNA. $n = 3$ technical repeats. Error bars represent ± SD. *, $P < 0.05$ by *t* test. **(G and H)** Dermal fibroblasts were isolated from Act1-deficient mice and retrovirally restored with wild-type Act1 or mutant Act that is defective in the ability to bind to mRNA (referred as 1+5mt; G). HLH, helix-loop-helix. Cells were then treated or not with IL-17A for indicated times followed by Western analysis (H). **(I)** Act1-deficient dermal fibroblasts restored with Act1 WT or Act1(1+5mt) were left untreated or treated with IL-17A, then subjected to hydroxyproline assay and LOX assay. $n = 3$ technical repeats. Error bars represent ± SEM. *, $P < 0.05$ by *t* test. Data are representative of at least three independent experiments for E–I.

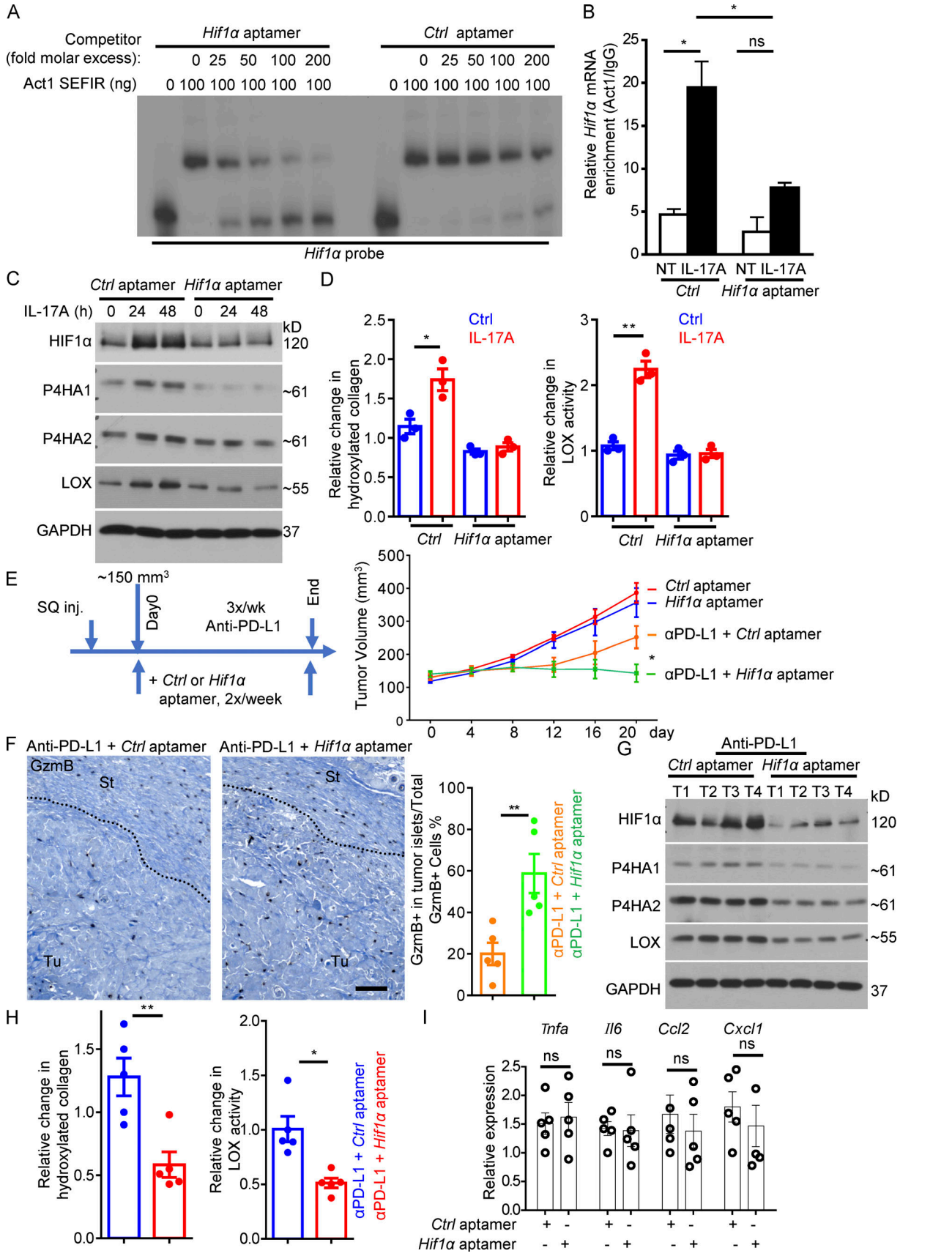

Figure 6. **Targeting IL-17 induced Act1-*Hif1α*-SBE interaction and reconditioned the TME for improved responses to anti–PD-L1. (A)** Competition REMSA of recombinant Act1 SEFIR domain using the *Hif1α* mRNA 3′ UTR SBE-containing region as a probe (Fig. 5 E) and either *Hif1α* aptamer or control

aptamer. **(B)** CAFs of DMBA/TPA-induced tumors transfected with control or *Hif1α* aptamers were treated with IL-17A for 8 h followed by anti-Act1 RIP and RT-PCR analysis for *Hif1α* mRNA. *n* = 3 technical repeats. Error bars represent ± SD. *, P < 0.05 by *t* test. **(C)** CAFs of DMBA/TPA-induced tumors transfected with control or *Hif1α* aptamers were then untreated or treated with IL-17A for indicated times followed by Western analysis. **(D)** CAFs of DMBA/TPA-induced tumors transfected with control or *Hif1α* aptamers were then untreated or treated with IL-17A, followed by hydroxyproline assay and LOX assay. *n* = 3 technical repeats. Error bars represent ± SEM. *, P < 0.05; **, P < 0.01 by *t* test. Data are representative of at least three independent experiments for A–D. **(E)** Tumor volumes from PDVC57 model over the time course of experiment with control or *Hif1α* aptamer. C57BL/6 mice with similar tumor size (five mice in each group) were used for indicated treatments. Error bars represent ± SEM. *, P < 0.05 by *t* test. SQ inj., subcutaneously injected. **(F)** Representative images of CD8 staining of tumors from anti–PD-L1 + *Ctrl* aptamer or anti–PD-L1 + *Hif1α* aptamer treated tumors from E. Scale bar, 100 µm. Bar graph represents GzmB+ cell ratio in the tumor islets over total $GzmB^+$ cells (in stroma and in tumor islets). Dotted lines are used to show the main boundary of tumor islets and stroma areas. *n* = 5 biological samples. Error bars represent ± SEM. **, P < 0.01 by *t* test. St, stroma; Tu, tumor islets. **(G and H)** Western analysis of indicated proteins (G) and hydroxyproline assay and LOX assay (H) in tumor lysates from control aptamer or *Hif1α* aptamer treated tumors that had been under immunotherapy (anti–PD-L1) from endpoint of E. *n* = 5. Error bars represent ± SEM. *, P < 0.05; **, P < 0.01 by *t* test. Each lane indicates an individual sample. **(I)** Relative mRNA level of indicated gene expression in PDVC57 tumors treated with control or *Hif1α* aptamer together with anti–PD-L1. *n* = 5 biological samples. Error bars represent ± SEM. *t* test. Data are representative of two independent experiments for E–I.

which IL-17 may acquire versatile regulatory functions by directly activating diverse master transcription factors.

Of interest, IL-17 signaling was recently shown to promote the metabolic reprogramming and proliferation of fibroblastic reticular cells, a type of specialized fibroblasts found in secondary lymphoid tissues (Majumder et al., 2019). Our data show that while IL-17–induced HIF1α expression may partially contribute to some IL-17–induced metabolic changes, HIF1α is dispensable for IL-17–induced CAF proliferation. Complementing our observations, IL-17–induced IκBζ has been shown to play a critical role in driving metabolic reprogramming (Majumder et al., 2019). Collectively, the evidence implies that IL-17–induced expression of HIF1α and IκBζ may synergistically regulate fibroblasts activation by stimulating their proliferation, metabolic reprogramming, and collagen deposition.

A critical question raised by our finding is how collagen deposition impedes the infiltration of cytotoxic T cells. The stromal entrapment of T cells has been shown to independently predict response to anti–PD-L1 in urothelial cancer (Mariathasan et al., 2018). Mechanistically, it was suggested that the dense collagen fiber in tumor stroma could override chemokine-directed T cell migration, thus abrogating chemotaxis toward the tumor cells (Hartmann et al., 2014). Additionally, mounting evidence shows that the stiff tumor stroma is a physical barrier that impedes normal T cell trafficking (Kuczek et al., 2019; Nicolas-Boluda et al., 2021). Furthermore, collagen may also promote the "exhausted phenotype" of cytotoxic T cells via the collagen receptor LAIR1, which is expressed on activated CD8 T cells (Peng et al., 2020). Taken together, collagen deposition can mediate immune exclusion via a multitude of pathways.

Checkpoint blockade–mediated augment of Th17 response has been reported in cancer patients (Dulos et al., 2012). Echoing this observation, anti–PD-L1 treatment leads to an upregulation of IL-17 in the tumor in our study. Furthermore, we show that IL-17 signaling in CAFs is required for the continued accumulation of collagen during tumor progression and for the maintenance of LOX activity in fibrotic tumor. Thus, IL-17 blockade may represent a viable strategy to prevent therapy-induced collagen deposition. A number of IL-17–targeting biologics are currently approved by the U.S. Food and Drug Administration for rheumatic diseases. These IL-17–targeting therapies exhibit a relatively favorable safety profile, and in isolated cases, have been prescribed to checkpoint blockade–treated cancer patients for associated immunotoxicities (Johnson et al., 2019; Mazzarella et al., 2020). Data from this study provide a strong rationale for repurposing existing IL-17–targeting agents to be used in conjunction with checkpoint blockade to prevent tumor fibrosis and subsequent therapy failure.

Growing evidence suggests that the stiffness of tumor stroma, a feature dependent on LOX-mediated crosslinking of collagen, has an outsized influence on T cell trafficking. A recent study showed that inhibition of LOX in human tumor explant improved the ability of T cells to traverse the tumor stroma, with similar levels of collagen in response to anti-PD1 (Nicolas-Boluda

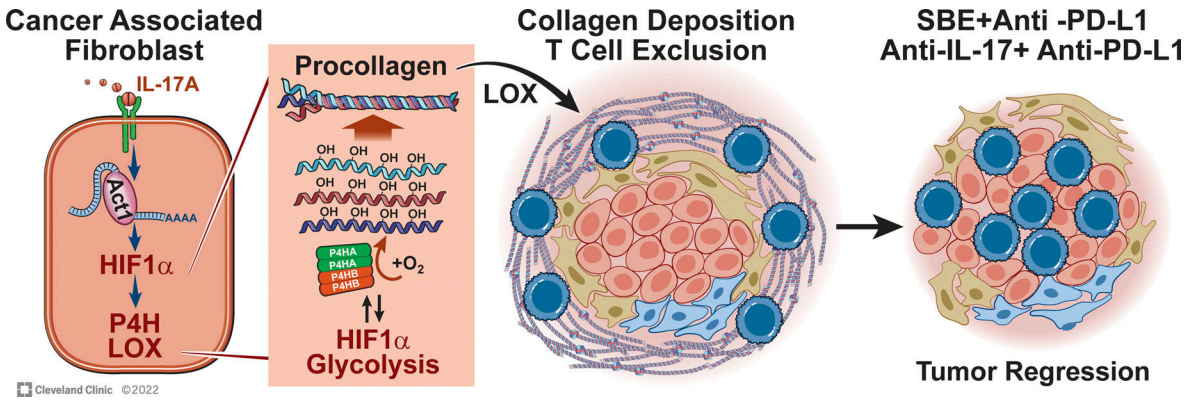

Figure 7. **Model for the IL-17–induced, Act1-promoted, HIF1α-mediated collagen deposition program.**

et al., 2021). Collectively, our study advocates a potential strategy to improve T cell infiltration in predeposited collagen fibers by disrupting the maintenance of LOX activity via IL-17 blockade.

Lastly, perhaps the most exciting demonstration of this study is the use of oligo-based agent to recondition TME. The RNA-based therapeutic platform is witnessing a revolution in both delivery and efficacy. We showed that Act1-targeting aptamer with *Hif1α* SBE sequence could be used as an effective and convenient tool to shut down the collagen-deposition program in the tumor, which potentiated the efficacy of anti–PD-L1. These data suggested that targeting mRNA metabolism may be a viable strategy for cancer treatment. Considering the advantages of manufacturing and the ease of reconfiguration with RNA-based therapies compared with antibody- or small molecule–based therapeutics, our data advocate a new approach to targeting TME and cancer immunotherapy.

Materials and methods

Animals

All experiments were conducted in accordance with Institutional Animal Care and Use Committee guidelines at the Cleveland Clinic Lerner Research Institute. The Col1a2-CreERT2 (Zheng et al., 2002) and HIF1α floxed mice (Ryan et al., 2000) were purchased from The Jackson Laboratory. IL-17RC floxed mice were generated by Cyagen Biosciences, with loxP sites flanking exons 6–7 of *Il17rc*. Gender- and age-matched mice were used for all experiments.

To induce transient Cre activity, tumor-bearing mice were i.p. injected with TAM (~5 mg/25 g weight for single dose or ~1 mg/25 g weight, three doses as indicated, e.g., days 0, 7, and 14 of the syngeneic model) for each experiment.

DMBA/TPA skin cancer model and PDVC57 mouse syngeneic model

For the DMBA/TPA model, each mouse was shaved and topically applied with 200 µl of 100 µM DMBA (dissolved in acetone). 2 wk later, each mouse was topically treated with 30 µg TPA in acetone twice a week up to 26 wk. Tumor incidence and numbers were monitored weekly. For PDVC57 syngeneic tumor model, PDVC57 cells in Matrigel were subcutaneously injected into the flanks of each mouse (0.5 million each tumor). Tumor size was monitored. Anti–PD-L1 was injected i.p. (300 µg/mouse for DMBA/TPA model, 200 µg/mouse for syngeneic model at indicated frequency for each experiment). For CD8 depletion, anti-CD8 treatment (300 µg/mouse) was started 3 d before anti–PD-L1 treatment and then at one dose each week. Control antibody of the same isotype was used (see Reagents below). Aptamers (see sequences in REMSA below) generated by IDT were given i.t. at 1 nmol/mouse (~20 µl PBS per injection), 2× per week.

Cell culture

Primary dermal fibroblast isolation has been described previously (Lichti et al., 2008). Briefly, the dermis side of newborn mouse skin was floated on cold trypsin solution (0.25% without EDTA) at 4°C overnight. The epidermis was then removed, and the dermal fraction was further digested with 300 U/ml collagenase at 37°C for 30 min. Collected dermal fraction was minced (diluted with 5× volume PBS), triturated (by pipetting up and down), and further transferred to a 50-ml tube through 100-µm nylon mesh strainers. Cell suspension was then centrifuged at 450 *g* for 5 min at 4°C. The pellet was washed with culture medium once more and subjected to culture for further analysis in the presence of penicillin (100 U/ml) and streptomycin (100 µg/ml).

For cancer-associated fibroblasts, fresh tumors were cut into small pieces and dissociated with collagenase IV/hyaluronidase (300 and 200 U/ml) solution in RPMI 1640 with penicillin (100 U/ml) and streptomycin (100 µg/ml) at 37°C. Dead cells were removed by Ficoll-Paque. Sorted EpCAM-negative alive cells were further cultured in DMEM/F12 medium with 10% FBS. Medium was changed every other day until the fibroblasts expanded and made up >95% adhesive cells. For human CAFs, tumors were dissociated as described above, and dissociated cells were cryopreserved in liquid nitrogen for later recovery and CAF culture.

For Cre-mediated in vitro deletion, adenovirus expressing GFP or GFP/Cre recombinase was purchased from Vector Biolabs. Primary fibroblasts on day 1 (at low confluence) were infected with adenovirus (1:10,000) for 2 d. On day 3, cells were washed with PBS and cultured in fresh medium. Around day 5, cells were passaged for further studies. Mycoplasma-free cell culture was confirmed with a mycoplasma detection kit (MycoStrip mycoplasma detection kit; InvivoGen) before use. Lipofectamine RNAiMAX (Invitrogen; Thermo Fisher Scientific) was used for siRNA and aptamer transfection.

Flow cytometry analysis

Fresh tumors were cut into small pieces and dissociated with mouse tumor dissociation kit (Miltenyi). Dead cells were removed by Ficoll-Paque, and live cells were analyzed with indicated markers.

Western blot

Cell lysates were made as described previously (Chen et al., 2019). Briefly, cells were washed with ice-cold PBS three times and lysed in lysis buffer (1% Triton X-100, 50 mM Tris-HCl, pH 7.4, 150 mM NaCl, 12.5 mM β-glycerophosphate, 1.5 mM $MgCl_2$, 10 mM NaF, 2 mM dithiothreitol [DTT], 2 mM sodium orthovanadate, 2 mM EGTA, and protease inhibitor cocktail [Roche]). Cell extracts were centrifuged at 12,000 rpm for 10 min at 4°C. Protein concentration was normalized with Bio-Rad Protein Assay Kit (5000006) for further Western blot.

Immunohistochemistry and immunofluorescence staining

For paraffin sections, as described previously (Chen et al., 2019), tissues were fixed with 10% formalin overnight and then kept in 70% ethanol at 4°C until processed into paraffin blocks at Cleveland Clinic Imaging Core or AML Laboratories. Paraffin sections were subjected to deparaffinization and epitope retrieval recommended by the antibody manufacturer. Sections were further blocked for 2 h (PBS containing 2% donkey serum,

0.5% BSA, 0.5% fish skin gelatin, 0.05% Tween 20, and 0.1% Triton X-100, pH 7.2), followed by primary antibody incubation overnight for further immunohistochemistry or immunofluorescence staining. For immunohistochemistry staining, after primary antibody incubation, sections were treated with 0.3% H_2O_2, followed by incubation of biotinylated secondary antibodies and peroxidase Streptavidin (Vector Laboratories). DAB substrate kit from BD Pharmingen was used. For frozen tissue embedded in optimal cutting temperature blocks, sections were fixed with 4% paraformaldehyde for 20 min and washed with PBST (PBS and 0.025% Tween 20), followed by blocking buffer and antibody incubation. Unless otherwise specified, paraffin sections were used for staining. Images were captured with a DP71 digital camera (Lumenera's INFINITY1) attached to an Olympus BX41 microscope or with Keyence BZ-X700 microscope.

LOX activity assay and hydroxyproline assay

For all LOX activity assays (Lysyl oxidase Activity Assay Kit, ab112139; Abcam), products in the last step were incubated at 37°C extendedly up to 3 h and then measured at ~OD_{576} with a microplate reader (Molecular Devices). For hydroxylated collagen measurement, we assumed the majority of total hydroxyproline was derived from collagen (Elia et al., 2019), therefore hydroxyproline assay was performed for hydroxylated collagen based on the chloramine T–dimethylaminobenzaldehyde (DMAB) methods (Elia et al., 2019). Data are presented as relative fold-change of LOX activity and hydroxylated collagen, or OD value per milligram protein where necessary.

Reagents and related information

Aniline Blue was part of the Trichrome Stain Kit (ab150686; Abcam). Picrosirius Red Stain Kit was from Polysciences, Inc. (24901-500).

Antibodies for Western blot (WB) and staining: anti-HIF1α for WB (36169, 1:1,000; Cell Signaling); anti-HIF1α for staining (sc-13515, 1:100; Santa Cruz); anti-P4HA1for WB (ab244400, 1:1,000; Abcam; or 12658-1-AP, 1:1,000; Proteintech); anti-P4HA2 for WB (CL0351, 1:1,000; Novus; or 66604-1-Ig, 1:1,000; Proteintech); anti-LOX for WB (58135, 1:1,000; Cell Signaling); anti-HK2 for WB (ab209847, 1:1,000; Abcam); anti-CPT1a for WB (ab128568, 1:1,000; Abcam); Act1 antibody for RIP (sc-398161, 1:100; Santa Cruz); anti-mouse CD8 for staining (ab217344, 1:200; Abcam); anti-ki67 for staining (14-5698, SolA15, 1:150; Invitrogen); anti-human CD8 for staining (85336, 1:100; Cell Signaling); anti-mouse IL-17A for staining (A00421-2, 1:150; Boster); anti-human IL-17A for staining (AF-317, 1:50; R&D); anti-GzmB for staining (NB100-684, validated in mouse, 1:150; Novus); anti-CD45 for staining (AF114, 1:150; R&D); and anti-mouse Gr-1 for staining (550291, clone RB6-8C5, 1:100; BD Pharmingen, frozen section only).

Antibodies for flow cytometry were all used at ~0.25 µg per 10^6 cells in each 100-µl volume: anti-CD8 for flow cytometry (clone 53-6.7; BioLegend); anti-GzmB for flow cytometry (clone QA16A02; BioLegend); anti-CD45 for flow cytometry (clone 30-F11; BioLegend); anti-PD1 for flow cytometry (clone 29F.1A12; BioLegend); and anti-Ki67 for flow cytometry (clone 11F6; BioLegend).

In vivo antibodies: anti–PD-L1 for in vivo injection (10F.9G2; BioXCell), controlled by rat IgG2b (LTF-2; BioXCell); anti-CD8 for depletion (2.43; BioXCell), controlled by rat IgG2b (LTF-2; BioXCell); anti–IL-17A for in vivo injection (17F3; BioXCell), controlled by mouse IgG1 (MOPC-21; BioXCell).

IL-17A and IL-17F used for comparison of IL-17 effects in fibroblast were obtained from Peprotech (210-17 and 210-17F); recombinant mouse IL-17A protein (421-ML; R&D) and recombinant human IL-17A protein (317-ILB; R&D) were used for all other stimulations.

siRNAs used for *Hif1α* knockdown were from Dharmacon (Horizon); *Si-Hif1α*, used with a mixture of ON-TARGETplus human *Hif1α* siRNA J-004018-07 and J-004018-08; and *Si-ctrl*, ON-TARGETplus D-001810 (Doe et al., 2012).

RIP assay

The RIP assay for the ability of Act1 to bind to RNA was described previously (Herjan et al., 2018). Briefly, 1 × 10^7 fibroblasts with indicated treatment were left untreated or treated with IL-17A (50 ng/ml) for 10 h. Cells were then trypsinized, washed twice, and resuspended in 10 ml ice-cold PBS. Cells were fixed in 0.1% formaldehyde for 15 min at room temperature, whereupon the cross-linking reaction was stopped with glycine (pH 7; 0.25 M). The cells were then washed twice with ice-cold PBS, resuspended in 2 ml radioimmunoprecipitation assay buffer (50 mM Tris-HCl, pH 7.5, 1% NP-40, 0.5% sodium deoxycholate, 0.05% SDS, 1 mM EDTA, 150 mM NaCl, and protease inhibitors), and sonicated. The lysate was centrifuged (15 min, 4°C, 16,000 *g*), and 1 ml of each supernatant was immunoprecipitated overnight at 4°C, using Dynabeads (Invitrogen) preincubated with anti-Act1 or IgG. The beads were washed five times with 1 ml radioimmunoprecipitation assay buffer and resuspended in 150 µl elution buffer (50 mM Tris-HCl, pH 7, 5 mM EDTA, 10 mM DTT, and 1% SDS). Cross-linking was reversed by incubation at 70°C for 45 min, RNA was purified from immunoprecipitates with Trizol (Invitrogen) according to the manufacturer's instructions and treated with RNase-free DNase. cDNAs were synthesized, and 10% (2 µl) of the reverse transcriptase product was subjected to quantitative real-time PCR.

REMSA

The methods for probe preparation, REMSA, and aptamer competition were developed and described previously (Herjan et al., 2018). Briefly, to prepare 3′ UTR *Hif1α* probe, fragments containing the mouse 3′ UTR *Hif1α* were generated by PCR and cloned into the pGEM-3ZF(+) vector (Promega) through the EcoRI and BamHI sites. All mutations were introduced with a QuikChange II Site Directed Mutagenesis Kit (Stratagene) according to the manufacturer's instructions. Purified protein at indicated concentration and labeled probes (10 fmol) were combined in the binding buffer for 30 min. The final REMSA binding buffer concentrations were 140 mM KCl, 10 mM Hepes, pH 7.9, 5% glycerol, 1 mM DTT, and 0.33 mg/ml tRNA. The reaction was further supplemented with 15 µg salmon sperm DNA to decrease nonspecific interactions from the lysate. Complexes were resolved on either 4% or 6% nondenaturing polyacrylamide

gels. The gels were dried, and the appearance of complexes was visualized by exposure to BioMax MR film. For *Hif1α* aptamer competition assay, the purified recombinant Act1 SEFIR was incubated with the ^{32}P-labeled mouse *Hif1α* 3′ UTR probes for 15 min to form protein–RNA complexes. For aptamer competition assay, *Hif1α* aptamers or control aptamers were added at indicated fold molar excess over the probe for an additional 10 min, then subjected to REMSA. The *Hif1α* aptamer (SBE) sequence used in this study was 5′-UAAUGCUCUUUUUAAUAUGUUCUUUUAAUGCCAGAUCACAGCACAUUCACAGCU-3′; control aptamer, which does not bind to Act1 SEFIR, was described previously (SBE mut C; Herjan et al., 2018).

Polysomal fractionation analysis

A total of 2 × 10^8 cells were left untreated or treated with IL-17A (50 ng/ml) for 8 h. Cytoplasmic exacts were then subjected to polysomal fractionation analysis as described previously (Herjan et al., 2013).

Human specimens

Use of deidentified human cutaneous SCC specimens was approved by the Institutional Review Board of the Cleveland Clinic Foundation with all necessary consents from patients. Specimens were randomly selected from a cohort collected from surgeries to remove skin tumors or skin tumor metastasis that were diagnosed as SCCs from 2015 to 2019.

Quantification and statistical analysis

Statistical significance was determined as described for each experiment. For all the *t* tests, P values were obtained from two-tailed tests from two groups with assumed unequal variances. All the data are representative of repeated experiments as described separately.

Online supplemental material

Fig. S1 shows that IL-17A neutralization sensitizes cutaneous SCC to anti–PD-L1–mediated regression. Fig. S2 shows the fibroblast proliferation status in anti–PD-L1–treated tumors. Fig. S3 shows that IL-17 induced HIF1α expression and collagen deposition in human CAFs. Fig. S4 shows that ablation of IL-17 signaling in fibroblasts compromised hydroxylated collagen accumulation and LOX activity in the DMBA/TPA model. Primers used in the study are listed in Table S1.

Acknowledgments

The cell line PDVC57 was kindly provided by Dr. Allan Balmain at University of California, San Francisco, San Francisco, CA. Fig. 7 illustration was supported by David Schumick, BS, CMI, at Cleveland Clinic Center for Medical Art & Photography. Reprinted with permission, Cleveland Clinic Foundation ©2022. All Rights Reserved.

This study is supported by the U.S. National Institutes of Health (5P01CA062220 and 5P01 HL103453) and Paul Fox Endowed Chair Funding awarded to Xiaoxia Li; and National Institutes of Health 1R01HL144497-01A1 to C. Liu. This work was also supported by Case Western Reserve University through departmental startup funding awarded to Xiao Li.

Author contributions: X. Li, X. Li, X. Chen, J. Zhao, T. Herjan, and L. Hong designed and analyzed all the experiments. X. Chen, J. Zhao, T. Herjan, L. Hong, Y. Liao, C. Liu, H. Wang, and A. Thompson were involved in performing and analyzing multiple experiments. P.L. Fox and K. Vasu provided technical and equipment support for polysome fractionation. B.R. Gastman helped with human cSCC collection and gave consultation for experiment design. X. Li, X. Li, X. Chen, and J. Zhao wrote the paper with input from all co-authors. X. Li and X. Li supervised all aspects of the study.

Disclosures: T. Herjan, L. Hong, C. Liu, and Xiaoxia Li reported a patent to US20200157544A1 pending, a patent to EP3655007A4 pending, and a patent to CN111093678A pending. No other disclosures were reported.

Submitted: 30 March 2021
Revised: 1 February 2022
Accepted: 23 March 2022

References

Akbay, E.A., S. Koyama, Y. Liu, R. Dries, L.E. Bufe, M. Silkes, M.M. Alam, D.M. Magee, R. Jones, M. Jinushi, et al. 2017. Interleukin-17A promotes lung tumor progression through neutrophil attraction to tumor sites and mediating resistance to PD-1 blockade. *J. Thorac. Oncol.* 12: 1268–1279. https://doi.org/10.1016/j.jtho.2017.04.017

Amatya, N., E.E. Childs, J.A. Cruz, F.E.Y. Aggor, A.V. Garg, A.J. Berman, J.E. Gudjonsson, U. Atasoy, and S.L. Gaffen. 2018. IL-17 integrates multiple self-reinforcing, feed-forward mechanisms through the RNA binding protein Arid5a. *Sci. Signal.* 11:eaat4617. https://doi.org/10.1126/scisignal.aat4617

Bentovim, L., R. Amarilio, and E. Zelzer. 2012. HIF1alpha is a central regulator of collagen hydroxylation and secretion under hypoxia during bone development. *Development*. 139:4473–4483. https://doi.org/10.1242/dev.083881

Binnewies, M., E.W. Roberts, K. Kersten, V. Chan, D.F. Fearon, M. Merad, L.M. Coussens, D.I. Gabrilovich, S. Ostrand-Rosenberg, C.C. Hedrick, et al. 2018. Understanding the tumor immune microenvironment (TIME) for effective therapy. *Nat. Med.* 24:541–550. https://doi.org/10.1038/s41591-018s4150014-x

Buchmann, A., B. Ruggeri, A.J. Klein-Szanto, and A. Balmain. 1991. Progression of squamous carcinoma cells to spindle carcinomas of mouse skin is associated with an imbalance of H-ras alleles on chromosome 7. *Cancer Res.* 51:4097–4101.

Chen, J., and Z. Chen. 2014. The effect of immune microenvironment on the progression and prognosis of colorectal cancer. *Med. Oncol.* 31:82. https://doi.org/10.1007/s12032-014-0082-9

Chen, X., G. Cai, C. Liu, J. Zhao, C. Gu, L. Wu, T.A. Hamilton, C.J. Zhang, J. Ko, L. Zhu, et al. 2019. IL-17R-EGFR axis links wound healing to tumorigenesis in Lrig1(+) stem cells. *J. Exp. Med.* 216:195–214. https://doi.org/10.1084/jem.20171849

Doe, M.R., J.M. Ascano, M. Kaur, and M.D. Cole. 2012. Myc posttranscriptionally induces HIF1 protein and target gene expression in normal and cancer cells. *Cancer Res.* 72:949–957. https://doi.org/10.1158/0008-5472.CAN0008-511-2371

Dulos, J., G.J. Carven, S.J. van Boxtel, S. Evers, L.J.A. Driessen-Engels, W. Hobo, M.A. Gorecka, A.F.J. de Haan, P. Mulders, C.J.A. Punt, et al. 2012. PD-1 blockade augments Th1 and Th17 and suppresses Th2 responses in peripheral blood from patients with prostate and advanced melanoma cancer. *J. Immunother.* 35:169–178. https://doi.org/10.1097/CJI.0b013e318247a4e7

Elia, I., M. Rossi, S. Stegen, D. Broekaert, G. Doglioni, M. van Gorsel, R. Boon, C. Escalona-Noguero, S. Torrekens, C. Verfaillie, et al. 2019. Breast cancer cells rely on environmental pyruvate to shape the metastatic niche. *Nature.* 568:117–121. https://doi.org/10.1038/s41586-019s4150977-x

Gopalakrishnan, V., C.N. Spencer, L. Nezi, A. Reuben, M.C. Andrews, T.V. Karpinets, P.A. Prieto, D. Vicente, K. Hoffman, S.C. Wei, et al. 2018. Gut

microbiome modulates response to anti-PD-1 immunotherapy in melanoma patients. *Science*. 359:97–103. https://doi.org/10.1126/science.aan4236

Gu, F.M., Q. Gao, G.M. Shi, X. Zhang, J. Wang, J.H. Jiang, X.Y. Wang, Y.H. Shi, Z.B. Ding, J. Fan, and J. Zhou. 2012. Intratumoral IL-17(+) cells and neutrophils show strong prognostic significance in intrahepatic cholangiocarcinoma. *Ann. Surg. Oncol.* 19:2506–2514. https://doi.org/10.1245/s10434-012s1042268-8

Han, X., Q. Yang, L. Lin, C. Xu, C. Zheng, X. Chen, Y. Han, M. Li, W. Cao, K. Cao, et al. 2014. Interleukin-17 enhances immunosuppression by mesenchymal stem cells. *Cell Death Differ.* 21:1758–1768. https://doi.org/10.1038/cdd.2014.85

Hartmann, N., N.A. Giese, T. Giese, I. Poschke, R. Offringa, J. Werner, and E. Ryschich. 2014. Prevailing role of contact guidance in intrastromal T-cell trapping in human pancreatic cancer. *Clin. Cancer Res.* 20:3422–3433. https://doi.org/10.1158/1078-0432.CCR1078-013-2972

He, S., M. Fei, Y. Wu, D. Zheng, D. Wan, L. Wang, and D. Li. 2011. Distribution and clinical significance of Th17 cells in the tumor microenvironment and peripheral blood of pancreatic cancer patients. *Int. J. Mol. Sci.* 12:7424–7437. https://doi.org/10.3390/ijms12117424

Herjan, T., L. Hong, J. Bubenik, K. Bulek, W. Qian, C. Liu, X. Li, X. Chen, H. Yang, S. Ouyang, et al. 2018. IL-17-receptor-associated adaptor Act1 directly stabilizes mRNAs to mediate IL-17 inflammatory signaling. *Nat. Immunol.* 19:354–365. https://doi.org/10.1038/s41590-018s4150071-9

Herjan, T., P. Yao, W. Qian, X. Li, C. Liu, K. Bulek, D. Sun, W.P. Yang, J. Zhu, A. He, et al. 2013. HuR is required for IL-17–induced Act1-mediated CXCL1 and CXCL5 mRNA stabilization. *J. Immunol.* 191:640–649. https://doi.org/10.4049/jimmunol.1203315

Honzawa, Y., H. Nakase, M. Shiokawa, T. Yoshino, H. Imaeda, M. Matsuura, Y. Kodama, H. Ikeuchi, A. Andoh, and Y. Sakai, et al. 2014. Involvement of interleukin-17A-induced expression of heat shock protein 47 in intestinal fibrosis in Crohn's disease. *Gut.* 63:1902–1912. https://doi.org/10.1136/gutjnl-2013-305632

Huang, Y., F. Wang, Y. Wang, Z. Zhu, Y. Gao, Z. Ma, R. Xu, and Z. Du. 2014. Intrahepatic interleukin-17+ T cells and FoxP3+ regulatory T cells cooperate to promote development and affect the prognosis of hepatocellular carcinoma. *J. Gastroenterol. Hepatol.* 29:851–859. https://doi.org/10.1111/jgh.12418

Johnson, D., A.B. Patel, M.I. Uemura, V.A. Trinh, N. Jackson, C.M. Zobniw, M.T. Tetzlaff, P. Hwu, J.L. Curry, and A. Diab. 2019. IL17A blockade successfully treated psoriasiform dermatologic toxicity from immunotherapy. *Cancer Immunol. Res.* 7:860–865. https://doi.org/10.1158/2326-6066.CIR2326-618-0682

Kim, T.K., R.S. Herbst, and L. Chen. 2018. Defining and understanding adaptive resistance in cancer immunotherapy. *Trends Immunol.* 39:624–631. https://doi.org/10.1016/j.it.2018.05.001

Kuczek, D.E., A.M.H. Larsen, M.L. Thorseth, M. Carretta, A. Kalvisa, M.S. Siersbæk, A.M.C. Simoes, A. Roslind, L.H. Engelholm, E. Noessner, et al. 2019. Collagen density regulates the activity of tumor-infiltrating T cells. *J. Immunother. Cancer.* 7:68. https://doi.org/10.1186/s40425-019-0556-6

Lichti, U., J. Anders, and S.H. Yuspa. 2008. Isolation and short-term culture of primary keratinocytes, hair follicle populations and dermal cells from newborn mice and keratinocytes from adult mice for in vitro analysis and for grafting to immunodeficient mice. *Nat. Protoc.* 3:799–810. https://doi.org/10.1038/nprot.2008.50

Liu, C., R. Liu, B. Wang, J. Lian, Y. Yao, H. Sun, C. Zhang, L. Fang, X. Guan, J. Shi, et al. 2021. Blocking IL-17A enhances tumor response to anti-PD-1 immunotherapy in microsatellite stable colorectal cancer. *J. Immunother. Cancer.* 9:e001895. https://doi.org/10.1136/jitc-2020-001895

Llosa, N.J., B. Luber, A.J. Tam, K.N. Smith, N. Siegel, A.H. Awan, H. Fan, T. Oke, J. Zhang, J. Domingue, et al. 2019. Intratumoral adaptive immunosuppression and type 17 immunity in mismatch repair proficient colorectal tumors. *Clin. Cancer Res.* 25:5250–5259. https://doi.org/10.1158/1078-0432.CCR1078-019-0114

Majumder, S., N. Amatya, S. Revu, C.V. Jawale, D. Wu, N. Rittenhouse, A. Menk, S. Kupul, F. Du, I. Raphael, et al. 2019. IL-17 metabolically reprograms activated fibroblastic reticular cells for proliferation and survival. *Nat. Immunol.* 20:534–545. https://doi.org/10.1038/s41590-019s4150367-4

Malhotra, V., and P. Erlmann. 2015. The pathway of collagen secretion. *Annu. Rev. Cell Dev. Biol.* 31:109–124. https://doi.org/10.1146/annurev-cellbio-100913-013002

Mariathasan, S., S.J. Turley, D. Nickles, A. Castiglioni, K. Yuen, Y. Wang, E.E. Kadel III, H. Koeppen, J.L. Astarita, R. Cubas, et al. 2018. TGFbeta attenuates tumour response to PD-L1 blockade by contributing to exclusion of T cells. *Nature*. 554:544–548. https://doi.org/10.1038/nature25501

Mazzarella, L., S. Giugliano, P. D'Amico, C. Belli, B.A. Duso, M. Rescigno, and G. Curigliano. 2020. Evidence for interleukin 17 involvement in severe immune-related neuroendocrine toxicity. *Eur. J. Cancer.* 141:218–224. https://doi.org/10.1016/j.ejca.2020.10.006

Meng, F., K. Wang, T. Aoyama, S.I. Grivennikov, Y. Paik, D. Scholten, M. Cong, K. Iwaisako, X. Liu, M. Zhang, et al. 2012. Interleukin-17 signaling in inflammatory, Kupffer cells, and hepatic stellate cells exacerbates liver fibrosis in mice. *Gastroenterology*. 143:765–776.e3. https://doi.org/10.1053/j.gastro.2012.05.049

Mucciolo, G., C. Curcio, C. Roux, W.Y. Li, M. Capello, R. Curto, R. Chiarle, D. Giordano, M.A. Satolli, R. Lawlor, et al. 2021. IL17A critically shapes the transcriptional program of fibroblasts in pancreatic cancer and switches on their protumorigenic functions. *Proc. Natl. Acad. Sci. USA.* 118:e2020395118. https://doi.org/10.1073/pnas.2020395118

Myllyharju, J. 2003. Prolyl 4-hydroxylases, the key enzymes of collagen biosynthesis. *Matrix Biol.* 22:15–24. https://doi.org/10.1016/s0945-053x(03)00006-4

Myllyharju, J. 2008. Prolyl 4-hydroxylases, key enzymes in the synthesis of collagens and regulation of the response to hypoxia, and their roles as treatment targets. *Ann. Med.* 40:402–417. https://doi.org/10.1080/07853890801986594

Nicolas-Boluda, A., J. Vaquero, L. Vimeux, T. Guilbert, S. Barrin, C. Kantari-Mimoun, M. Ponzo, G. Renault, P. Deptula, K. Pogoda, et al. 2021. Tumor stiffening reversion through collagen crosslinking inhibition improves T cell migration and anti-PD-1 treatment. *Elife.* 10:e58688. https://doi.org/10.7554/eLife.58688

Park, M.-J., S.-J. Moon, E.-J. Lee, K.-A. Jung, E.-K. Kim, D.-S. Kim, J.-H. Lee, S.-K. Kwok, J.-K. Min, S.-H. Park, and M.L. Cho. 2018. IL-1-IL-17 signaling axis contributes to fibrosis and inflammation in two different murine models of systemic sclerosis. *Front. Immunol.* 9:1611. https://doi.org/10.3389/fimmu.2018.01611

Peng, D.H., B.L. Rodriguez, L. Diao, L. Chen, J. Wang, L.A. Byers, Y. Wei, H.A. Chapman, M. Yamauchi, C. Behrens, et al. 2020. Collagen promotes anti-PD-1/PD-L1 resistance in cancer through LAIR1-dependent CD8(+) T cell exhaustion. *Nat. Commun.* 11:4520. https://doi.org/10.1038/s41467-020-18298-8

Punt, S., E.A. Dronkers, M.J. Welters, R. Goedemans, S. Koljenovic, E. Bloemena, P.J. Snijders, A. Gorter, S.H. van der Burg, R.J. Baatenburg de Jong, and E.S. Jordanova. 2016. A beneficial tumor microenvironment in oropharyngeal squamous cell carcinoma is characterized by a high T cell and low IL-17(+) cell frequency. *Cancer Immunol. Immunother.* 65:393–403. https://doi.org/10.1007/s00262-016-1805-x

Punt, S., J.M. Langenhoff, H. Putter, G.J. Fleuren, A. Gorter, and E.S. Jordanova. 2015. The correlations between IL-17 vs. Th17 cells and cancer patient survival: a systematic review. *Oncoimmunology*. 4:e984547. https://doi.org/10.4161/2162402X.2014.984547

Quintanilla, M., S. Haddow, D. Jonas, D. Jaffe, G.T. Bowden, and A. Balmain. 1991. Comparison of ras activation during epidermal carcinogenesis in vitro and in vivo. *Carcinogenesis*. 12:1875–1881. https://doi.org/10.1093/carcin/12.10.1875

Robert, C. 2020. A decade of immune-checkpoint inhibitors in cancer therapy. *Nat. Commun.* 11:3801. https://doi.org/10.1038/s41467-020-17670-y

Rossow, L., S. Veitl, S. Vorlova, J.K. Wax, A.E. Kuhn, V. Maltzahn, B. Upcin, F. Karl, H. Hoffmann, S. Gatzner, et al. 2018. LOX-catalyzed collagen stabilization is a proximal cause for intrinsic resistance to chemotherapy. *Oncogene*. 37:4921–4940. https://doi.org/10.1038/s41388-018s4130320-2

Ryan, H.E., M. Poloni, W. McNulty, D. Elson, M. Gassmann, J.M. Arbeit, and R.S. Johnson. 2000. Hypoxia-inducible factor-1alpha is a positive factor in solid tumor growth. *Cancer Res.* 60:4010–4015

Sharma, P., S. Hu-Lieskovan, J.A. Wargo, and A. Ribas. 2017. Primary, adaptive, and acquired resistance to cancer immunotherapy. *Cell*. 168:707–723. https://doi.org/10.1016/j.cell.2017.01.017

Tan, Z., X. Qian, R. Jiang, Q. Liu, Y. Wang, C. Chen, X. Wang, B. Ryffel, and B. Sun. 2013. IL-17A plays a critical role in the pathogenesis of liver fibrosis through hepatic stellate cell activation. *J. Immunol.* 191:1835–1844. https://doi.org/10.4049/jimmunol.1203013

Tosolini, M., A. Kirilovsky, B. Mlecnik, T. Fredriksen, S. Mauger, G. Bindea, A. Berger, P. Bruneval, W.H. Fridman, F. Pages, and J. Galon. 2011. Clinical impact of different classes of infiltrating T cytotoxic and helper cells (Th1, th2, treg, th17) in patients with colorectal cancer. *Cancer Res.* 71:1263–1271. https://doi.org/10.1158/0008-5472.can-10-2907

Vallet, S.D., and S. Ricard-Blum. 2019. Lysyl oxidases: from enzyme activity to extracellular matrix cross-links. *Essays Biochem.* 63:349–364. https://doi.org/10.1042/EBC20180050

Wu, J., J. Du, L. Liu, Q. Li, W. Rong, L. Wang, Y. Wang, M. Zang, Z. Wu, Y. Zhang, and C. Qu. 2012. Elevated pretherapy serum IL17 in primary hepatocellular carcinoma patients correlate to increased risk of early recurrence after curative hepatectomy. *PLoS One*. 7:e50035. https://doi.org/10.1371/journal.pone.0050035

Xu, C., K. Hao, L. Yu, and X. Zhang. 2014. Serum interleukin-17 as a diagnostic and prognostic marker for non-small cell lung cancer. *Biomarkers*. 19: 287–290. https://doi.org/10.3109/1354750x.2014.908954

Yan, J., X.L. Liu, G. Xiao, N.L. Li, Y.N. Deng, L.Z. Han, L.C. Yin, L.J. Ling, and L.X. Liu. 2014. Prevalence and clinical relevance of T-helper cells, Th17 and Th1, in hepatitis B virus-related hepatocellular carcinoma. *PLoS One*. 9:e96080. https://doi.org/10.1371/journal.pone.0096080

Zhang, G.Q., F. Han, X.Z. Fang, and X.M. Ma. 2012. CD4+, IL17 and Foxp3 expression in different pTNM stages of operable non-small cell lung cancer and effects on disease prognosis. *Asian Pac. J. Cancer Prev.* 13: 3955–3960. https://doi.org/10.7314/apjcp.2012.13.8.3955

Zhang, Y., V. Chandra, E. Riquelme Sanchez, P. Dutta, P.R. Quesada, A. Rakoski, M. Zoltan, N. Arora, S. Baydogan, W. Horne, et al. 2020. Interleukin-17-induced neutrophil extracellular traps mediate resistance to checkpoint blockade in pancreatic cancer. *J. Exp. Med.* 217:e20190354. https://doi.org/10.1084/jem.20190354

Zhang, Y., Y. Huang, and M. Qin. 2013. Tumour-infiltrating FoxP3+ and IL-17-producing T cells affect the progression and prognosis of gallbladder carcinoma after surgery. *Scand. J. Immunol.* 78:516–522. https://doi.org/10.1111/sji.12109

Zhang, Y., M. Zoltan, E. Riquelme, H. Xu, I. Sahin, S. Castro-Pando, M.F. Montiel, K. Chang, Z. Jiang, J. Ling, et al. 2018. Immune cell production of interleukin 17 induces stem cell features of pancreatic intraepithelial neoplasia cells. *Gastroenterology*. 155:210–223.e3. https://doi.org/10.1053/j.gastro.2018.03.041

Zheng, B., Z. Zhang, C.M. Black, B. de Crombrugghe, and C.P. Denton. 2002. Ligand-dependent genetic recombination in fibroblasts: a potentially powerful technique for investigating gene function in fibrosis. *Am. J. Pathol.* 160:1609–1617. https://doi.org/10.1016/S0002-9440(10)61108-X

Supplemental material

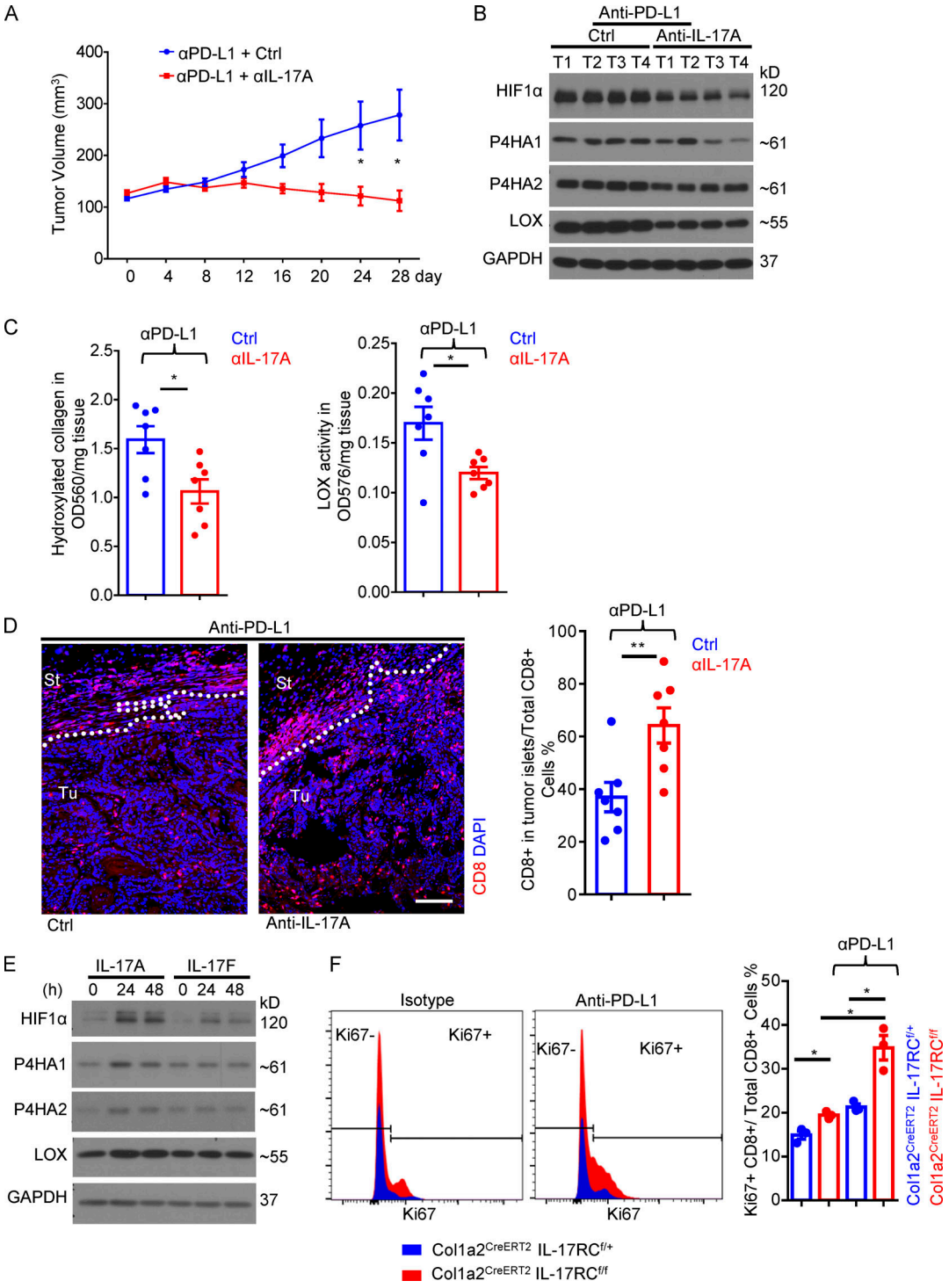

Figure S1. **IL-17A neutralization sensitizes cutaneous SCC to anti–PD-L1–mediated regression. (A)** Tumor volumes from PDVC57 cell–derived syngeneic model over the time course of anti–PD-L1 + isotype (Ctrl) or anti–PD-L1 + anti–IL-17A treatment. C57BL/6 mice with similar tumor size (seven mice in each group) were used for indicated treatments. Error bars represent ± SEM. *, P < 0.05 by *t* test. **(B)** Western analysis of tumor pieces from four random biological samples of A. **(C)** Hydroxyproline assay and LOX assay in tumor lysates (n = 7) from anti–PD-L1 + isotype (Ctrl) or anti–PD-L1 + anti–IL-17A neutralizing antibody treated mice in A. Error bars represent ± SEM. *, P < 0.05 by *t* test. **(D)** Representative images of CD8 staining of tumors from anti–PD-L1 + isotype (Ctrl) or anti–PD-L1 + anti–IL-17A neutralizing antibody treated mice in A. Bar graph represents the percentage of $CD8^+$ T cells in the tumor islets over the total $CD8^+$ T cells (in stroma and in tumor islets). n = 7 biological samples. Error bars represent ± SEM. **, P < 0.01 by *t* test. St, stroma; Tu, tumor islets. Dotted lines are used to show the main boundary of tumor islets and stroma areas. Scale bar = 100 µm. **(E)** Dermal fibroblasts were treated with IL-17A and IL-17F for indicated times followed by Western analysis. Data are representative of at least three independent experiments. **(F)** Tumor tissues from endpoint of PDVC57 model as described in Fig. 1 F with IL-17RC$^{f/+}$Col1a2^{CreERT2} or IL-17RC$^{f/f}$Col1a2^{CreERT2} mice were harvested, dissociated, and examined by flow cytometry analysis for indicated markers. Cells gated on $CD8^+$ were subjected to Ki67 analysis in histograms. Bar graph indicates $CD8^+Ki67^+$/total $CD8^+$ T cell ratio in the whole tumor from three independent specimens. Error bars represent ± SEM. *, P < 0.05 by *t* test. Data are representative of two independent experiments.

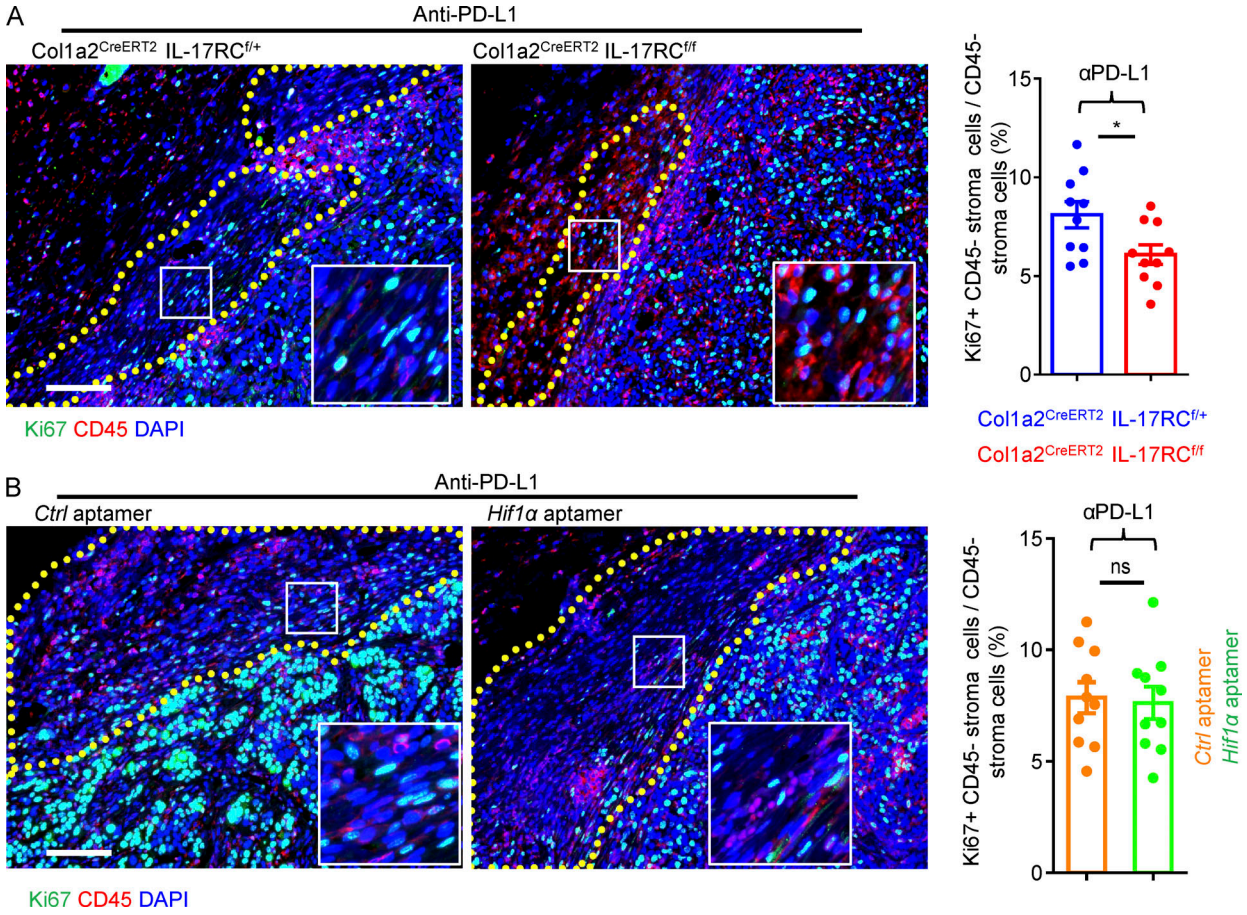

Figure S2. **Fibroblast proliferation status in anti–PD-L1–treated tumors. (A)** Paraffin sections of anti–PD-L1–treated PDVC57 tumors from indicated mice of Fig. 1 H were stained for proliferative marker Ki67 (green) and hematopoietic marker CD45 (red) and counterstained with DAPI (blue). Major stroma areas are demarcated with dotted lines. Bar graph shows percentages of $CD45^-$ cells with positive Ki67 nuclei staining in stromal areas from 10 fields of five biologically independent tumors. Error bars represent ± SEM. *, $P < 0.05$ by *t* test. **(B)** Representative staining of Ki67 (green), CD45 (red), and DAPI (blue) in tumors from Fig. 6E (mice treated with anti–PD-L1 and control [*Ctrl*] or *Hif1α* targeting aptamer). Major stroma areas are demarcated with dotted lines. Bar graph shows percentages of $CD45^-$ cells with positive Ki67 nuclei staining in stromal areas from 10 fields of five biologically independent tumors. Error bars represent ± SEM. *t* test.

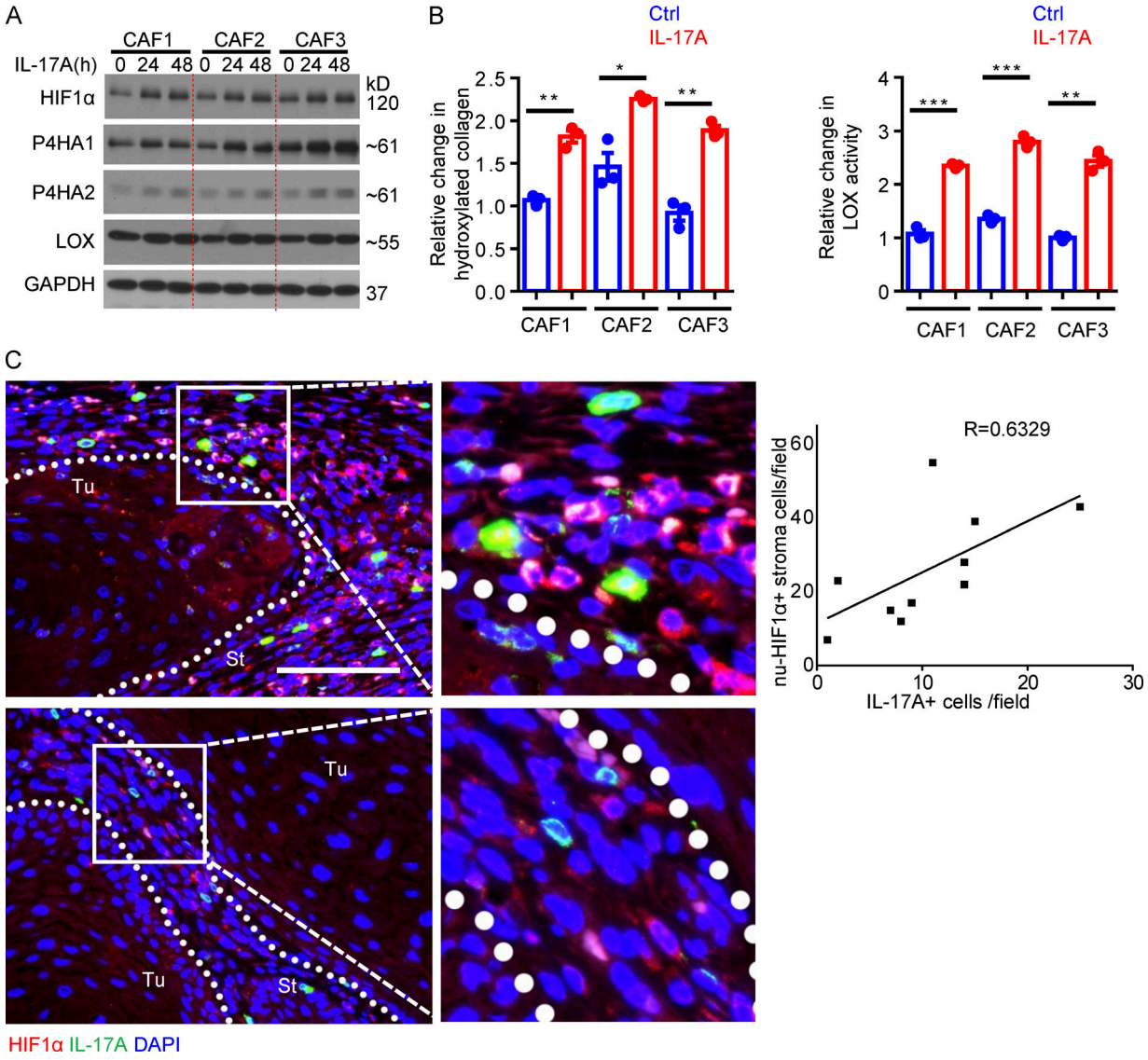

Figure S3. **IL-17 induced HIF1α expression and collagen deposition in human CAFs. (A)** Western blot analysis of IL-17A–treated CAFs for 24 and 48 h. **(B)** Hydroxyproline assay and LOX assay for IL-17A–treated and untreated (Ctrl) human CAFs (48 h). *n* = 3 technical repeats. Error bars represent ± SEM; *, P < 0.05; **, P < 0.01; ***, P < 0.001 by *t* test. CAFs for A and B were from three independent human cutaneous SCCs, and data are representative of three independent experiments. **(C)** Immunofluorescence analysis of IL-17A (green)–producing cells and HIF1α (red) expression in two representative cutaneous SCCs. Scale bar, 100 µm. St, stroma; Tu, tumor islets. Dotted lines are used to show the main boundary of tumor islets and stroma areas. Graph shows correlation of nuclear HIF1α-positive cells (nu-HIF1α+) and IL-17A–producing cells in random stroma areas (40× magnification) of 10 human cutaneous SCCs.

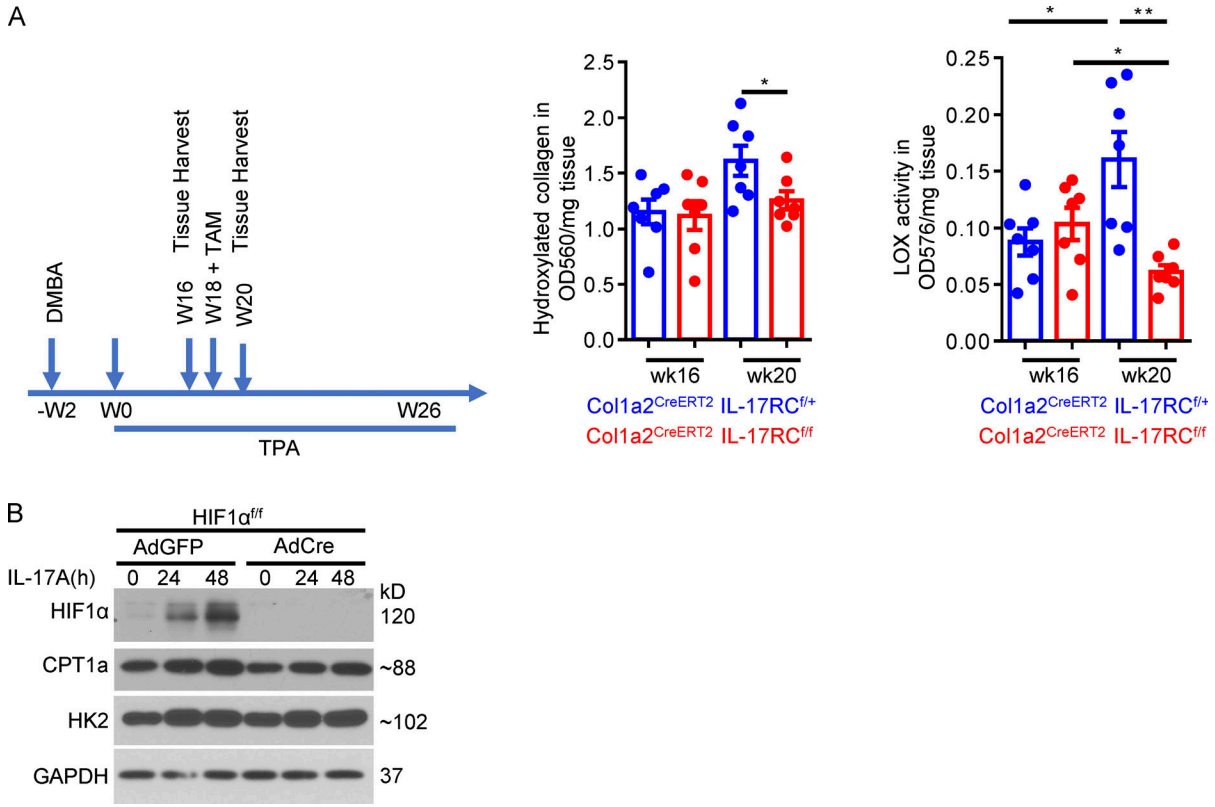

Figure S4. **Ablation of IL-17 signaling in fibroblasts compromised hydroxylated collagen accumulation and LOX activity in the DMBA/TPA model. (A)** Tumor tissues harvested from DMBA/TPA model of indicated genotype at week 16 (TAM untreated) and week 20 (TAM treated at week 18) were subjected to hydroxyproline assay and LOX assay. $n = 7$ independent specimens of three mice in each group. Error bars represent ± SEM. *, $P < 0.05$; **, $P < 0.01$ by t test. **(B)** Primary skin fibroblasts from HIF1α$^{f/f}$ mice were infected with adenovirus carrying vectors for either GFP (AdGFP) or Cre recombinase (AdCre) to generate control and HIF1α knockout fibroblasts. Infected cells were treated with IL-17A for indicated time and analyzed by Western blot. Western data are representative of three independent experiments.

Provided online is Table S1. Table S1 lists primers for gene expression analysis.